AGU PUBLICATIONS

JGR

Journal of Geophysical Research: Solid Earth

RESEARCH ARTICLE
10.1002/2017JB015138

Special Section:
Gas Hydrate in Porous Media: Linking Laboratory and Field Scale Phenomena

Archie's Saturation Exponent for Natural Gas Hydrate in Coarse-Grained Reservoirs

Ann E. Cook[1] and **William F. Waite**[2]

[1]School of Earth Science, The Ohio State University, Columbus, OH, USA, [2]U.S. Geological Survey, Woods Hole, MA, USA

Key Points:
- We develop a velocity-based gas hydrate saturation model to calibrate Archie's saturation exponent, *n*
- We find $n = 2.5 \pm 0.5$ applies to gas hydrate-bearing coarse-grained reservoirs in both marine and permafrost environments
- If possible, *n* should be calibrated using reservoir-specific data, but if those data are not available, $n = 2.5 \pm 0.5$ is recommended

Correspondence to:
A. E. Cook,
cook.1129@osu.edu

Citation:
Cook, A. E., & Waite, W. F. (2018). Archie's saturation exponent for natural gas hydrate in coarse-grained reservoirs. *Journal of Geophysical Research: Solid Earth*, *123*, 2069–2089. https://doi.org/10.1002/2017JB015138

Received 26 OCT 2017
Accepted 12 FEB 2018
Accepted article online 17 FEB 2018
Published online 11 MAR 2018

Abstract Accurately quantifying the amount of naturally occurring gas hydrate in marine and permafrost environments is important for assessing its resource potential and understanding the role of gas hydrate in the global carbon cycle. Electrical resistivity well logs are often used to calculate gas hydrate saturations, S_h, using Archie's equation. Archie's equation, in turn, relies on an empirical saturation parameter, *n*. Though $n = 1.9$ has been measured for ice-bearing sands and is widely used within the hydrate community, it is highly questionable if this *n* value is appropriate for hydrate-bearing sands. In this work, we calibrate *n* for hydrate-bearing sands from the Canadian permafrost gas hydrate research well, Mallik 5L-38, by establishing an independent downhole S_h profile based on compressional-wave velocity log data. Using the independently determined S_h profile and colocated electrical resistivity and bulk density logs, Archie's saturation equation is solved for *n*, and uncertainty is tracked throughout the iterative process. In addition to the Mallik 5L-38 well, we also apply this method to two marine, coarse-grained reservoirs from the northern Gulf of Mexico Gas Hydrate Joint Industry Project: Walker Ridge 313-H and Green Canyon 955-H. All locations yield similar results, each suggesting $n \approx 2.5 \pm 0.5$. Thus, for the coarse-grained hydrate bearing ($S_h > 0.4$) of greatest interest as potential energy resources, we suggest that $n = 2.5 \pm 0.5$ should be applied in Archie's equation for either marine or permafrost gas hydrate settings if independent estimates of *n* are not available.

1. Introduction

Natural gas hydrate contains a vast global store of methane, bound within sediments in marine continental slope and terrestrial permafrost environments. Gas hydrate is of interest as a possible source of commercial natural gas, with several countries investing in gas hydrate drilling and characterization (Boswell et al., 2012; Collett et al., 2014; Kumar et al., 2016; Ryu et al., 2013) as well as production tests (Kumar et al., 2016; Takahashi et al., 2005; Yamamoto et al., 2014). Gas hydrate is also a dynamic component of Earth's carbon cycle, capable of both storing and releasing methane. Methane release from dissociating natural gas hydrate has been tied to past and current climate change (Archer, 2007; Dickens, Castillo, & Walker, 1997) and could increase acidification and oxygen depletion in the ocean (Biastoch et al., 2011; Ruppel & Kessler, 2017).

Understanding the potential of gas hydrate as both a component of Earth's carbon cycle and as a gas resource relies on evaluating the amount of natural gas hydrate at global and reservoir scales. Because of uncertainties in hydrate distribution and saturation at a range of scales, global gas hydrate estimates vary by several orders of magnitude, ranging from nearly 10^{14} to 10^{17} m^3 of hydrate-bound natural gas. (Boswell & Collett, 2011; Johnson, 2011; Wallmann et al., 2012).

This work aims to improve constraints on hydrate saturation (S_h), the fraction of gas hydrate in the primary pore space, at the borehole scale using geophysical well logs. In practice, accurate S_h can be obtained from downhole point measurements utilizing pore water chlorinity as a hydrate saturation proxy (Malinverno et al., 2008; Ussler & Paull, 2001), or direct determination of S_h by measuring the gas volume produced during the dissociation of hydrate-bearing pressure cores (Dickens, Paull, & Wallace, 1997; Holland & Schultheiss, 2014; Konno et al., 2015; Lee et al., 2013). These point measurements, however, are not acquired with the continuous downhole coverage required to fully characterize a reservoir at a given site, nor are they acquired for every site.

Both electrical resistivity and compressional-wave velocity (V_p) are used to determine S_h and are typically collected in a well log suite at gas hydrate sites. Both properties increase as S_h increases (Pearson et al., 1983) because hydrate, with its relatively high resistivity (Du Frane et al., 2011) and high V_p (Helgerud et al., 2009), forms in the pore space of sands by displacing low resistivity, low V_p, pore water brine.

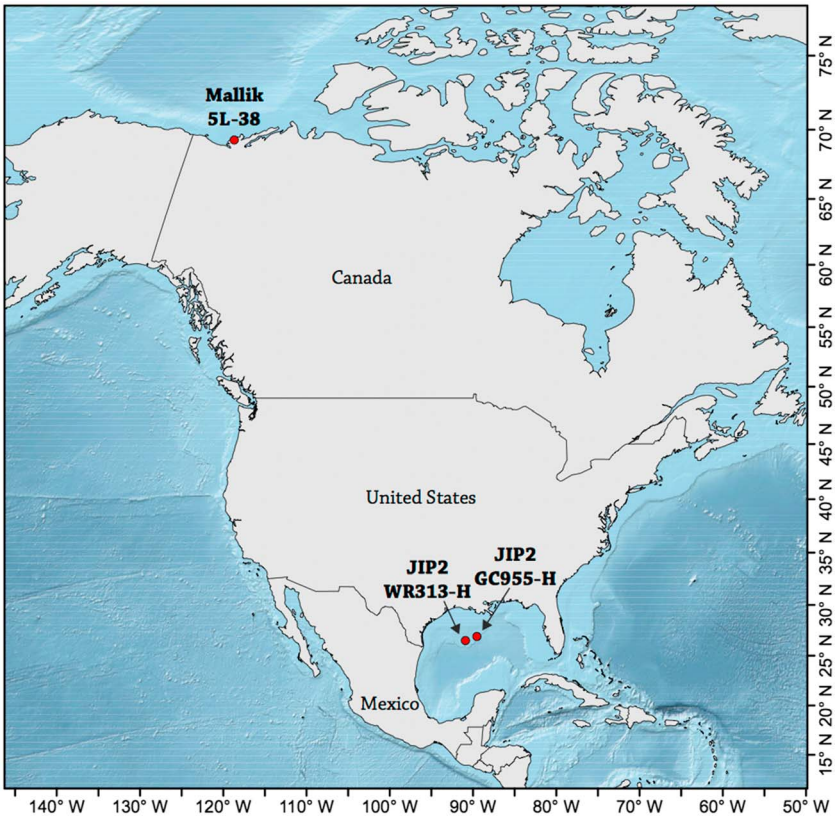

Figure 1. The location of the permafrost Mallik Gas Hydrate Production Research Well, Mallik 5L-38, in Northwest Territories, Canada, and two marine wells from the 2009 Gulf of Mexico Gas Hydrate Joint Industry Project: JIP2 WR313-H and JIP2 GC955-H. Bathymetry source: Esri (ArcGIS).

Resistivity, from either well logs or controlled source electromagnetic surveys, is routinely used to calculate S_h, (or water saturation $S_w = 1 - S_h$) using Archie's empirical saturation equation (e.g., Collett et al., 2012; Collett & Ladd, 2000; Goldberg et al., 2010; Pearson et al., 1983; Schwalenberg et al., 2010; Weitemeyer et al., 2011).

Archie's saturation equation (Archie, 1942), however, relies on an empirical hydrate saturation exponent, n, for which there is no consensus value applicable to sand or coarse silt reservoirs where hydrate forms in the primary pore space; we refer to these reservoirs that meet both the grain size and the pore-filling requirement as "coarse grained" in this work. Herein, n is calibrated in coarse-grained hydrate-bearing reservoirs based on a downhole S_h profile calculated from V_p well logs using the load-bearing model of Dvorkin et al. (2000) and supplemented with additional well log and core data. By looking at three different sites, one primary case site the Canadian permafrost, Mallik 5L-38, and two supporting marine sites in the Gulf of Mexico (Figure 1), $n = 2.5 \pm 0.5$ is found to be the best value to apply in Archie's equation to calculate S_h. This n value is recommended when core or other required parameters to calibrate Archie's n are not available in coarse-grained reservoirs. Establishing a general, site-independent value for n increases the utility and reliability of resistivity-based characterizations of these potential energy resources.

2. Existing Constraints on Archie's Equation and *n*

The electrical conductivity (the inverse of electrical resistivity), σ_o, in porous, brine-saturated reservoirs is controlled by two components (e.g., Waxman & Smits, 1968; Winsauer & McCardell, 1953; Worthington, 1985):

$$\sigma_o = \frac{1}{F}\sigma_w + \sigma_s. \quad (1)$$

The first component is the basis of Archie's equation and depends on the conductivity of the pore water brine, σ_w, and the formation factor, F, which describes the pore network in coarse-grained reservoirs

(Archie, 1942). The second component, $\sigma_{s,}$ is the contribution of the surface conductivity due to electrical conduction within a nanometer-scale region at the surface of silica grains or at the fluid/grain interface (Revil et al., 1998, 2014). Significant surface conductivity can occur in clay-rich sediment (Waxman & Smits, 1968) or with conductive minerals such as pyrite (Clavier et al., 1976; Clennell et al., 2010).

When equation (1) is applied in coarse-grained quartz reservoirs, the σ_s component is usually assumed to be negligible. Recently, however, Revil et al. (2014) demonstrated that even high-porosity clay-free sand could have a nonnegligible surface conductivity that is a function of S_w. In these situations, surface conductivity can become an increasingly large component of the bulk conductivity when the presence of an electrical insulator, such as hydrate, displaces pore water brine, thereby lowering the S_w and restricting the electrical path through the brine. For our primary test case of the Mallik 5L-38 sand reservoir, we show in Appendix A that surface conductivity is negligible, even as S_w decreases.

The dielectric permittivity of the sediment and pore constituents can also influence conductivity measurements, and these effects depend on measurement frequency (Knight & Nur, 1987; Sen et al., 1981). Most sediment, such as quartz, has very low dielectric permittivity. Pore constituents such as gas hydrate and water have a similar, high dielectric permittivity. At the electromagnetic wave well log frequencies used in this study (~100 kHz, 400 kHz, and 2 MHz), dielectric permittivity is accounted for during processing using a simple function that accounts for the porosity (Ellis & Singer, 2007; Wu et al., 1999). Moreover, electromagnetic resistivity tools have a suite of sensors that differ in measurement frequency and formation penetration depth. A strong dielectric material will impact each sensor differently, distorting the relationships between sensor readings observed in traditional environments (Anderson et al., 2007). None of the sites discussed here show evidence of dielectric effects on the resistivity logs, so this component is assumed to not affect the resistivity logs.

Thus, for the high-porosity, brine-saturated coarse-grained reservoirs considered in this work, σ_s and dielectric contributions are assumed negligible and only the first component of equation (1) is used.

When working with well logs or controlled source electromagnetic data, results are generally reported in terms of resistivity, R, the inverse of conductivity ($R = 1/\sigma$), and this convention is used hereafter. Archie (1942) expressed the resistivity of a coarse-grained, fully brine-saturated reservoir, $\mathscr{R}_o$, as a relationship between the intrinsic formation factor, F, and pore water resistivity, $\mathscr{R}_w$:

$$\mathscr{R}_o = F\mathscr{R}_{w,} \tag{2}$$

where

$$F = \frac{1}{\phi^m}. \tag{3}$$

The intrinsic formation factor describes the pore network as a function of porosity, ϕ, and porosity exponent, m. The value of m typically ranges between 1.4 and 2.2 and increases with angularity of the sand grain shape (Jackson et al., 1978). The value m is independent of hydrate saturation and is calibrated in adjacent water-filled coarse-grained intervals prior to investigating hydrate-bearing intervals, as described in Ellis and Singer (2007, p. 656). A second Archie parameter a is sometimes used in the numerator of equation (3) (Winsauer et al., 1952); we choose not to use it here as this allows equations (2) and (3) to be theoretically correct as ϕ approaches 1.

To calculate S_h using Archie's equation, denoted here as $S_{h-\mathscr{R}}$ to indicate hydrate saturation derived from resistivity, the ratio of the background or brine-saturated resistivity $\mathscr{R}_o$ (equations (2) and (3)) to the measured resistivity $\mathscr{R}$ is scaled by Archie's saturation exponent, n (Archie, 1942):

$$S_{h-\mathscr{R}} = 1 - \left(\frac{\mathscr{R}_o}{\mathscr{R}}\right)^{\frac{1}{n}}. \tag{4}$$

Archie n values are generally calibrated in a laboratory by measuring resistivity on a reservoir sample at multiple oil or gas saturations; n values in these reservoirs are related to saturation, wettability, microporosity, and clay content (Swanson, 1985; Sweeney & Jennings, 1960; Waxman & Smits, 1968). In coarse-grained hydrate reservoirs, calibrating n is still a very difficult task because the laboratory measurement must mimic the natural environment and replicate the natural pore space hydrate morphology. Like oil and gas reservoirs,

the value for n in hydrate environments is reservoir dependent, varying based on sediment pore shape, pore connectivity, distribution of conductive pore water and morphology of the resistive hydrate phase (Spangenberg, 2001). In fact, Spangenberg (2001) showed through several models that n could range from 0.5 to 4 in hydrate reservoirs, though this range spanned both pore-filling and fracture-filling hydrate accumulations.

Pearson et al. (1983) presented the first estimate of the saturation exponent for gas hydrate using water ice as an analog, estimating a best fit $n = 1.9386$ as a "pooled estimate" for several lithologies that included sandstone, limestone, and unconsolidated sediment. Over the last three decades, Pearson's value, $n \approx 1.9$, has become widely used within the gas hydrate community, though often without recognizing the result was based on studies of ice, or even that Pearson's work was the original source. For example, Waite et al. (2009) tabulated a selection of Archie n values from 13 different papers and 11 of the 13 papers used $n \approx 1.9$. Based on Waite et al. (2009), it may appear that there is community consensus on the Archie n value, but in all 11 cases where $n \approx 1.9$, the n value could be traced back, sometimes through multiple publications, to the original ice-based work of Pearson et al. (1983). Moreover, in none of the cases tabulated by Waite et al. (2009) was the value of n independently determined or factors such as surface conductivity considered.

More recent laboratory-based n calibrations present conflicting results. In one, a glass bead specimen suggested that $n \approx 2$ may work for $S_h < 0.5$ but that a calibration for n may not be possible for higher hydrate saturations (Spangenberg & Kulenkampff, 2006). On the other hand, Santamarina and Ruppel (2008) calibrated n on several different sediment types by using varying S_h of tetrahydrofuran hydrate. They found a best fit of $n \approx 1.6$, which included sand specimens with S_h exceeding 0.5.

In a separate calibration of n, Malinverno et al. (2008) used a novel field-based approach for a thin-sand layer in which a pore water chlorinity measurement was coupled with resistivity well logs from Integrated Ocean Drilling Program Expedition 311 on Cascadia Margin. A chlorinity-derived $S_h = 0.55$ was determined from a single pore water measurement in one thin-sand interval. The values for R_o and R were determined from well logs, and equation (4) was solved for n, producing $n = 2.42 \pm 0.28$ for the 9 cm thick sand (Malinverno et al., 2008).

The proper calibration of n is important because of its significant influence on the resulting S_h (equation (4)). To illustrate, Figure 2 (Track e) shows the calculated S_h using a range of n values from 1.5 to 3.5 for a hydrate-filled sand reservoir from the Mallik 5L-38 well. Within the hydrate-bearing sand, saturation calculated with $n = 3.5$ produces the lowest calculated values, with an average S_h of 0.52, while $n = 1.5$ produces the highest values, with an average S_h of 0.80.

3. Evidence Supporting the Load-Bearing Model

Models relating V_p to S_h are classified according to conceptual geometrical models the hydrate morphology within the pore space. Dvorkin et al. (2000) developed analytical models for four end-member pore space hydrate morphologies: pore-filling, load-bearing, surrounding cement and contact cement. Of these models, the load-bearing model of Dvorkin et al. (2000) has been independently validated in laboratory and field studies of marine and permafrost-associated hydrate-bearing reservoirs (Kleinberg et al., 2005; Konno et al., 2015; Lee & Collett, 2011; Santamarina et al., 2015). For example, in pressure cores from the Nankai Trough, S_h calculated using the load-bearing Dvorkin et al.'s. (2000) model from V_p measurements were in agreement with colocated, direct measurements of S_h based on gas and water volumes collected from controlled depressurizations of gas hydrate-bearing sands (Konno et al., 2015; Santamarina et al., 2015). The Dvorkin et al. (2000) load-bearing model is analytical, with no free or empirical parameters and thus has no need for recalibration in each new site. The model therefore has broad applicability for field and laboratory studies of gas hydrate, with the caveats that the reservoir must be coarse-grained so that hydrate forms in existing pore space, and the hydrate saturation must exceed 0.4.

In the marine environment, most coarse-grained hydrate-bearing reservoirs likely form from methane dissolved in sediment pore water (Collett et al., 2009). In these dissolved-gas, or gas-limited systems, hydrate tends to form away from sediment grain contacts (Tohidi et al., 2001). At low S_h, the hydrate and sediment may not interact mechanically at all. Of the Dvorkin et al. (2000) end-member models, this "pore-filling" distribution demonstrates the smallest stiffening and wave velocity increase effect for a given S_h. As S_h increases above ~0.4 (Lee et al., 2010; Yun et al., 2005), hydrate interacts with sediment grains and support additional

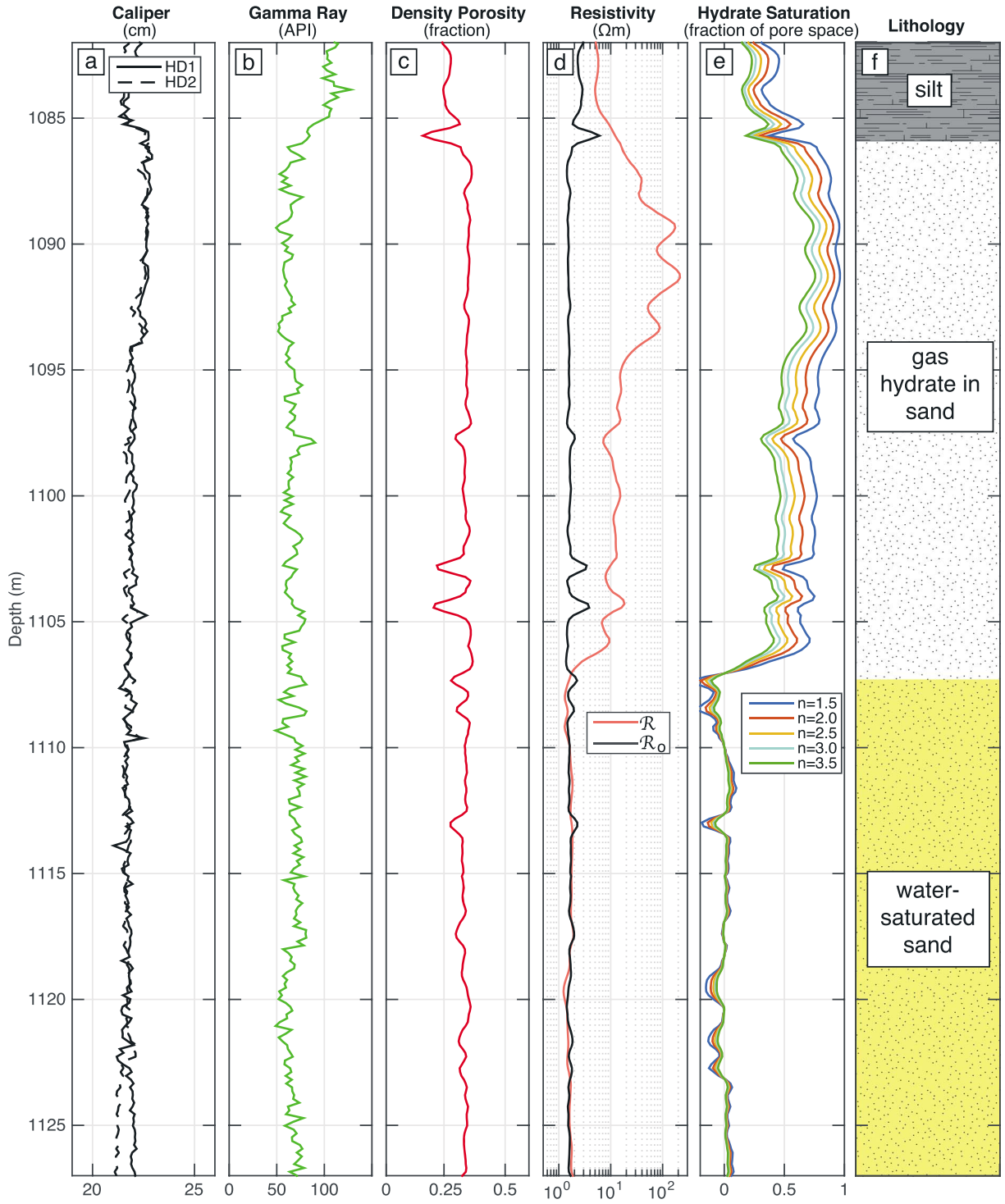

Figure 2. Archie's saturation equation (equation (4)) applied to well logs through a sand section from the Mallik 5L-38 well, using a range of values for the saturation exponent (n). Measured well logs are shown on Tracks a and b. Density is converted to density porosity on Track c using equation (7). Track d shows the measured AHF10 resistivity ($\mathscr{R}$), as well as the calculated background resistivity, $\mathscr{R}_o$ (equations (2) and (3)). In Track e, gas hydrate saturation (S_h) is calculated for a range of n values, from 1.5 to 3.5 (equation (4)), which results in a large range of S_h in the hydrate-bearing sand. Track f is lithology interpreted from the gamma ray and resistivity logs.

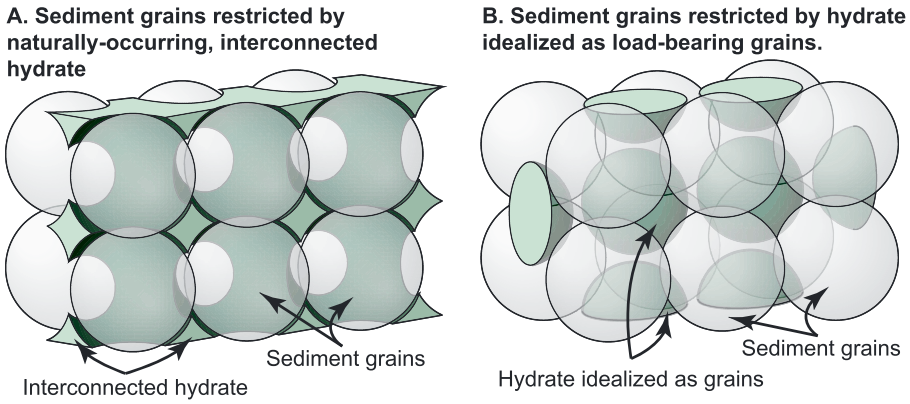

Figure 3. Schematic diagram of hydrate (green) within idealized sediment (gray spheres). As imaged by Kerkar et al. (2014) and Chaouachi et al. (2015), hydrate and sediment are separated by a water layer (shown here as a gap between hydrate and sediment). Nonetheless, the interconnected nature of hydrate between pores can provide the cohesion observed in coarse-grained hydrate-bearing reservoirs (Yoneda et al., 2017). (b) For the small strains generated during compressional wave velocity, V_p, tests, grain movement restrictions imposed by interconnected hydrate (a) can be analytically estimated by assuming hydrate simply acts as additional, load-bearing grains (green spheres) in the sediment (gray spheres) (Dvorkin et al., 2000).

loads or deformation imposed on the sediment. These "load-bearing" interactions stiffen the sediment and increase V_p for a given S_h more significantly than does the pore-filling arrangement (Lee et al., 2010; Priest et al., 2009; Spangenberg & Kulenkampff, 2005; Yun et al., 2005).

Physically, hydrate does not directly contact sediment grains, because a layer of water exists between hydrate and sediment grains whether hydrate forms from the dissolved-phase in an excess water environment (Kerkar et al., 2014), or from the gas phase in an excess gas environment (Chaouachi et al., 2015). In spite of the absence of direct hydrate/sediment contact, the interconnected nature of hydrate between pores spaces (Figure 3a; see also Figure 10 in Kerkar et al., 2014) acts to restrict sediment grain movement and hold sediment together. Interconnected hydrate provides the cohesion observed in naturally occurring hydrate-bearing sediment (Yoneda et al., 2017). For the small strains imposed during a V_p measurement, the sediment stiffening effects of "load-bearing" hydrate are analytically modeled by simplifying the hydrate distribution and treating hydrate as additional, load-bearing grains in the sediment (Figure 3b).

The load-bearing model is also valid for high S_h coarse-grained reservoirs in permafrost environments, though the load-bearing pore space hydrate morphology likely occurs only after a two-step formation process in which hydrate initially forms in water-limited, excess-gas systems, but then becomes water flooded (Collett et al., 2009; Dai et al., 2011). In a water-limited environment, water tends to collect at sediment grain contacts via capillary action. Conversion of water to hydrate bonds sediment grains together, dramatically stiffening the sediment and significantly increasing V_p even at a low S_h of a few percent (Priest et al., 2005; Waite et al., 2004), in what Dvorkin et al. (2000) term as "cementing" hydrate distributions. Subsequent water flooding likely caused the cementing hydrate morphology to evolve into a load-bearing morphology (Collett et al., 2009; Dai et al., 2011). This evolution from the elevated V_p levels characteristic of cementation to lower values characteristic of load-bearing hydrate during water flooding has been observed in laboratory studies (Choi et al., 2014; Ebinuma et al., 2005).

At Mallik 5L-38, a permafrost environment, the load-bearing model has been validated using nuclear magnetic resonance (NMR) well logs (Kleinberg et al., 2005). Figure 4 shows a comparison between hydrate saturation determined from Dvorkin et al.'s. (2000) load-bearing model ($S_{h\text{-}Vp}$), NMR logs ($S_{h\text{-NMR}}$), and from nonpressurized cores for Mallik 5L-38. $S_{h\text{-NMR}}$ is calculated using the methods of Kleinberg et al. (2005) and Goldberg et al. (2010). NMR porosity, called TCMR (total combined magnetic resonance porosity), is sensitive to the free hydrogen in molecules of pore water but not sensitive to hydrogen in water molecules bound in hydrate. Thus, TCMR porosity is approximately equal to the hydrate-free portion of the in situ pore space. Effectively, the porosity difference between the total porosity and the NMR-derived TCMR porosity (see Figure 4a) is used to calculate $S_{h\text{-NMR}}$ (Figure 4c).

There is robust agreement between $S_{h\text{-NMR}}$ and $S_{h\text{-}Vp}$ in the hydrate-saturated sand, especially in the thick, high saturation interval from 1,087 to 1,097 m (Figure 4). Small differences within this interval are most

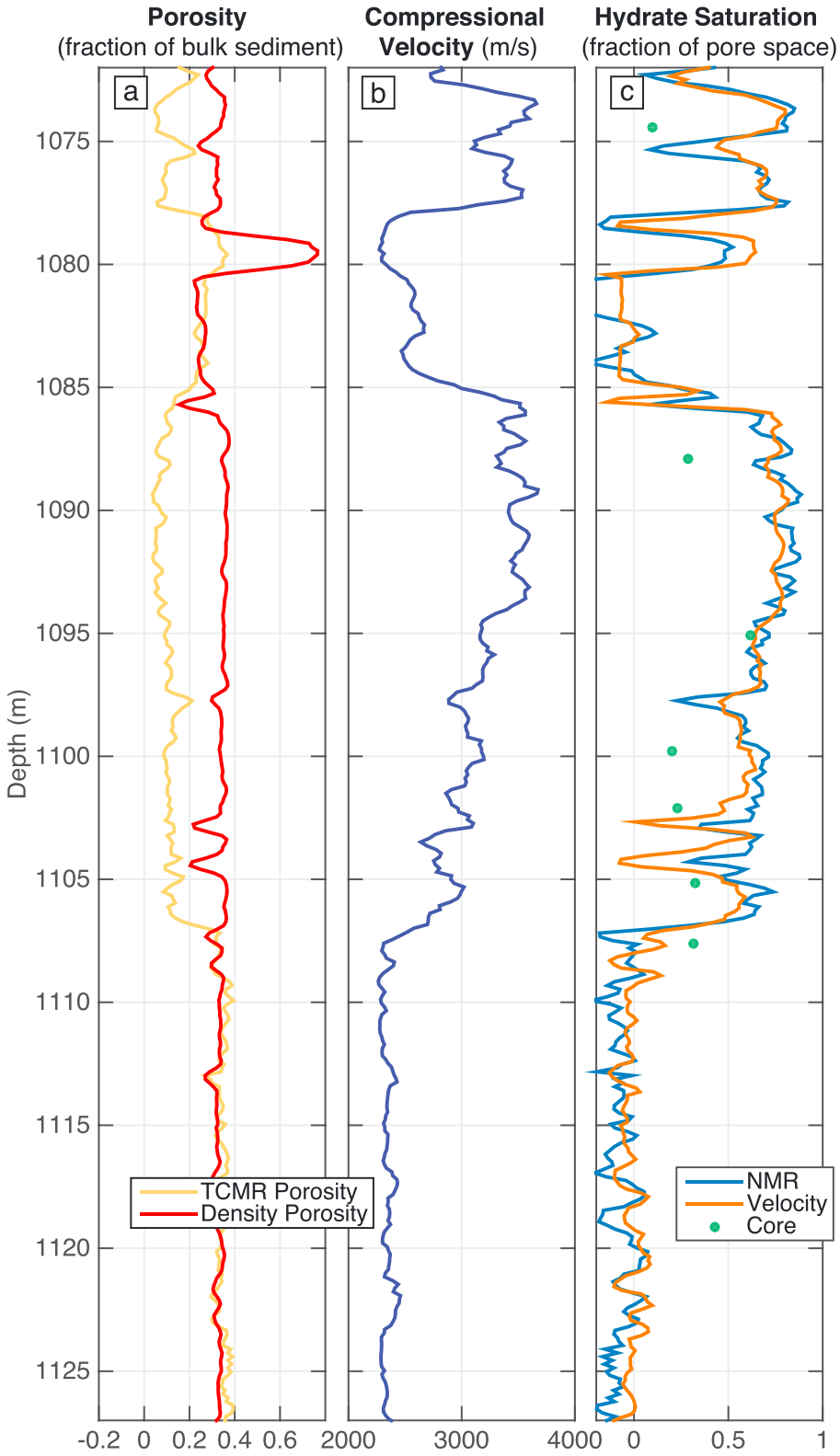

Figure 4. Validating the load-bearing V_p model estimates of hydrate saturation for Mallik 5L-38 against nuclear magnetic resonance (NMR) and nonpressurized core-based estimates. Track a shows the calculated density porosity (total porosity) and the total combined magnetic resonance (TCMR) porosity from the NMR measurement. TCMR is not sensitive to the pore space taken up by gas hydrate. Track b displays the measured compressional velocity. Track c displays gas hydrate saturation calculations from NMR, compressional velocity, and saturations estimated from nonpressurized core (Kleinberg et al., 2005; Lu et al., 2005). As Figure 4c indicates, $S_{h\text{-NMR}}$, and $S_{h\text{-}Vp}$ would be suitable for calibrating Archie's n.

likely the result of higher vertical resolution of the NMR measurement. Poor agreement also occurs where the lithology deviates from sand. For example, one poor match coincides with a coal bed from 1,079 to 1,080.5 m. Other mismatches at 1,085.5 m, 1,103 m, and 1,104.5 m coincide with sharp drops in porosity, which are likely thin carbonate-cemented layers or clay layers (Medioli et al., 2005). As Figure 4c illustrates, it is important to limit the application of the load-bearing V_p model to the coarse-grained lithology assumed in the model derivation (Dvorkin et al., 2000).

Direct measurements of S_h from the controlled depressurization of pressure-core-preserved hydrate-bearing sands are not available at Mallik 5L-38. Lu et al. (2005) measured gas volumes produced from conventional, nonpressurized core as residual gas hydrate dissociated on specimens that were held outside the gas hydrate stability conditions. Thus, unlike the pressure core results, the dissociation measurements from Lu et al. (2005) only capture a portion of the dissociating gas and thus underpredict the in situ hydrate saturation (green dots in Figure 4c) relative to both $S_{h\text{-NMR}}$ and $S_{h\text{-}Vp}$. Only one point at 1,107 m appears to overpredict S_h relative to $S_{h\text{-NMR}}$ and $S_{h\text{-}Vp}$. This measurement may be related to incorrect depth matching or to measurement resolution. In any case, these points are not used to calibrate n as they underestimate S_h at most depths.

The V_p log was chosen herein to calibrate n for two reasons. First, V_p logs are more commonly measured than NMR logs at scientific drilling and gas hydrate sites, which allows for additional comparison and application of this method beyond Mallik. Second, a resistivity log exists that explores an overall volume of the formation that is quite similar to what is measured with the V_p tool: the V_p was measured with the Schlumberger DSI (denotes mark of Schlumberger) tool, which records wave traveltimes with a ~1.1 m vertical resolution and a 23 cm average depth of investigation (Schlumberger, 2014) and the AHF10 induction resistivity log was acquired with the Schlumberger AIT tool that has a ~1.2 m vertical resolution and a ~25 cm depth of investigation (Schlumberger, 2004).

4. Methodology for Calibrating Archie's *n*

The calibration of n is based on solving equation (4) for n,

$$n = \frac{\log(\mathscr{R}_o) - \log(\mathscr{R})}{\log\left(1 - S_{h-V_p}\right)}, \tag{5}$$

which relies on the measured AHF10 resistivity log, $\mathscr{R}$, the calculated background resistivity, $\mathscr{R}_o$, (equation (2)), and an independent S_h (Malinverno et al., 2008). We determine the independent hydrate saturation profile, $S_{h\text{-}Vp}$, from the V_p log. This section describes how the S_h-$_{Vp}$ and $\mathscr{R}_o$ parameters are obtained and how uncertainty is determined. The Figure 5 flowchart summarizes the required steps and equations to solve for equation (5).

4.1. Calculating $S_{h\text{-}Vp}$

Compressional-wave velocity logs can be used to estimate hydrate saturation because the measurements are sensitive to changes in the sediment's bulk and shear moduli, which increase as the hydrate saturation increases. Compressional-wave velocity, V_p, is related to these moduli through

$$V_p = \sqrt{\frac{K_b + \frac{4}{3}G_b}{\rho_b}}, \tag{6}$$

where K_b and G_b are, respectively, the bulk and shear moduli of the total sediment, hydrate, and pore fluid system. The bulk density, ρ_b, is obtained from the bulk density log measurement.

Porosity, ϕ, is also a critical parameter connecting V_p to hydrate saturation, and ϕ is calculated from the bulk density log. This calculation of density porosity accounts for the density of water, ρ_w, the grain density ρ_g, and the hydrate density, ρ_h, (Table 1):

$$\phi = \frac{\rho_g - \rho_b}{\left(\rho_g - \rho_w - S_{h-Vp}(\rho_h - \rho_w)\right)} \tag{7}$$

$S_{h\text{-}Vp}$ is not known a priori, so porosity is initially calculated assuming $S_{h\text{-}Vp} = 0$. Porosity is then updated iteratively with each new estimate of $S_{h\text{-}Vp}$ (Figure 5).

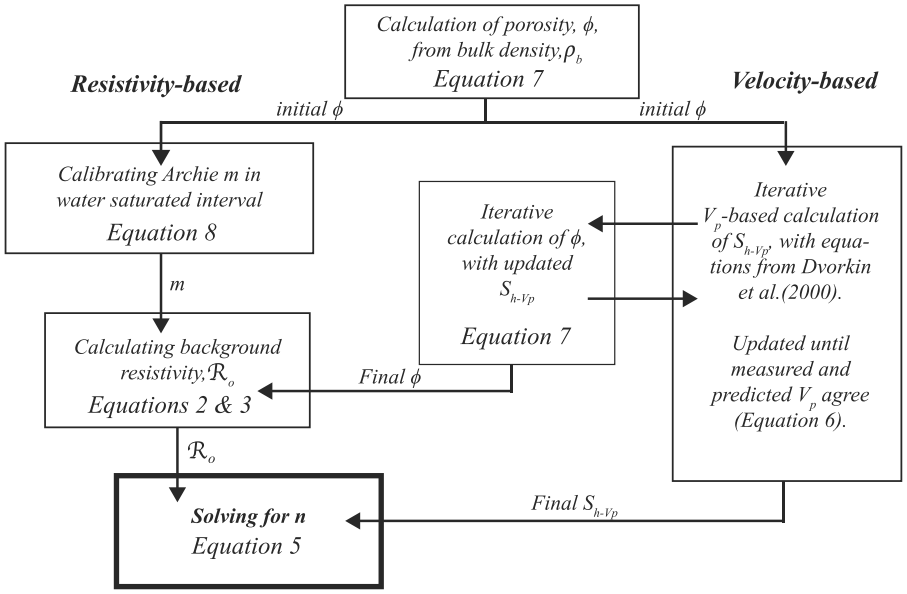

Figure 5. A flowchart showing the equation numbers and steps (indicated by arrows) used for solving for Archie's saturation exponent, *n*.

Table 1
Parameters and Uncertainties Used to Calibrate Archie's Saturation Exponent n for the Mallik 5L-38 Well

Symbol	Parameter	Units	Value and uncertainty (± 1δ)	Source
ρ_q	Sand grain density	g/cm^3	2.660 ± 0.016	Measured directly on cores from the Mallik 5L-38 sand interval (Winters et al., 2005)
ρ_w	Pore water density	g/cm^3	1.02 ± 0.01	Calculated using method of Batzle and Wang (1992) from measured Mallik 5L-38 values of salinity Winters et al. (2005) and temperature Henninges et al. (2005)
ρ_w	Methane hydrate density	g/cm^3	0.924 ± 0.028	Helgerud et al. (2009)
K_b	Quartz bulk modulus	GPa	38.4 ± 1.1	Pabst and Gregorova (2013)
K_w	Pore water bulk modulus	GPa	2.3 ± 0.1	Calculated using method of Batzle and Wang (1992) from measured Mallik 5L-38 values of salinity Winters et al. (2005) and temperature Henninges et al. (2005)
K_h	Methane hydrate bulk modulus (GPa)	GPa	8.4 ± 0.5	Helgerud et al. (2009)
G_q	Quartz shear modulus (GPa)	GPa	44.1 ± 0.5	Pabst and Gregorova (2013)
G_w	Pore water shear modulus (GPa)	GPa	0	True for fluids
G_h	Methane hydrate shear modulus (GPa)	GPa	3.54 ± 0.14	Helgerud et al. (2009)
ρ_b	Bulk density measurement	g/cm^3	±0.015 g/ cm^3	From Schlumberger brochure on Multiexpress (Schlumberger, 2009)
$\mathscr{R}_m$	Measured resistivity	Ωm	±2%	From Schlumberger brochure on the AIT Tool (Schlumberger, 2004)
V_p	Velocity measurement	m/s	±45 m/s	From Schlumberger brochure on the DSI tool (Schlumberger, 2014) (±2 μs/ft),
ϕ_c	Critical porosity	Fraction of bulk sediment	0.38 ± 0.02	Dvorkin et al. (1999); Nur et al. (1998)
$\mathscr{R}_w$	Water resistivity	Ωm	0.25 ± 0.02	Estimated from the Mallik 5L-38 salinity of Winters et al. (2005) and temperature Henninges et al. (2005)
m	Archie's porosity exponent	Unitless	1.70 ± 0.10	Calibrated in the water-saturated interval of Mallik 5L-38 from 1,109 to 1,136 m depth (this work)

Note. Values used for the Gulf of Mexico locations are presented in the text.

There are five main steps in Dvorkin et al. (2000) load-bearing modeling for connecting V_p, through the elastic moduli and density from equation (6), to $S_{h\text{-}Vp}$. First, because hydrate is assumed to act as a load-bearing sediment grain, the bulk and shear moduli of the sediment mineral, K_{min} and G_{min}, respectively, are calculated as the Hill average (Hill, 1952) using the quartz and hydrate moduli given in Table 1; an estimated $S_{h\text{-}Vp}$ is chosen for the initial iteration. Second, the bulk and shear moduli of the dry sediment frame, K_{HM} and G_{HM}, are calculated using the Hertz-Mindlin contact theory (Mindlin, 1949) at the in situ effective pressure. For this step, the sediment porosity is set at the critical porosity, ϕ_c, which is the threshold porosity below which sediment grains become load bearing. In coarse-grained systems, ϕ_c is 0.38 (Table 1) (Dvorkin et al., 1999; Nur et al., 1998). In the third step, dry sediment moduli, K_{dry} and G_{dry}, are calculated by combining the frame moduli at ϕ_c (K_{HM} and G_{HM} from step two) with the moduli of the hydrate + quartz grains (K_{min} and G_{min} from step one). The frame and grain moduli are combined using the modified lower Hashin-Shtrikman bound (Dvorkin and Nur, 1996). The proportion of grain material added to the critical porosity frame is chosen so as to reduce the overall sediment porosity from the critical porosity, ϕ_c from step two, to the calculated porosity, ϕ (equation (7)). The proportion of hydrate in the sediment grain material is determined in step one from the assumed $S_{h\text{-}Vp}$. Forth, the moduli of the water-saturated, hydrate-bearing frame, K_b and G_b, are calculated using the Gassmann (1951) equation to saturate the dry frame (K_{dry} and G_{dry}) with water having moduli of K_w and G_w (see Table 1). In the fifth step, V_p is calculated from equation (6) given the calculated bulk moduli, K_b and G_b, and the measured bulk density, ρ_b.

Rather than inverting these five steps to calculate $S_{h\text{-}Vp}$ from measured values of V_p, $S_{h\text{-}Vp}$ is corrected iteratively until the calculated and measured values of V_p match to the third significant figure (Figure 5). When $S_{h\text{-}Vp}$ is iterated, porosity is updated using equation (7). In this way, the final match of modeled and measured V_p provides a downhole profile of hydrate saturation, $S_{h\text{-}Vp}$, and porosity ϕ, for calculating n.

4.2. Calculating Archie's Exponent, *m*

The calculation of m is performed using data from hydrate-free, water-saturated coarse-grained interval adjacent to the hydrate-bearing interval. From equations (2) and (3), and assuming $a = 1$, m can be expressed as (as shown in Malinverno et al. (2008)):

$$m = \frac{\log(\mathscr{R}_w) - \log(\mathscr{R}_o)}{\log(\phi)}. \tag{8}$$

For the Mallik 5L-38 case, the sand formation is water saturated from 1,109 to 1,127 m (Figure 2). Within this hydrate-free interval, R_o is equal to the measured AHF10 resistivity. The pore water resistivity, R_w, is given in Table 1. The porosity, ϕ, is density derived, calculated from equation (7) and applying $S_{h\text{-}Vp} = 0$ because the interval is water saturated.

Based on the measured resistivity in the water-saturated sand and the parameter values from Table 1, $m = 1.7 \pm 0.1$. The uncertainty is based on the input parameter uncertainties as discussed in section 4.4. The value of m used for the supporting Gulf of Mexico sites are discussed in the results.

4.3. Calculating the Background Resistivity, $\mathscr{R}_o$

R_o in hydrate-bearing sands is calculated from equations (2) and (3). The pore water resistivity, R_w, is calculated based on temperature and salinity measured at the Mallik site and increased pressure with depth using the equations of Fofonoff & Millard (1983) (Table 1). The value for Archie's m is calculated as discussed in section 4.2, and porosity used is hydrate corrected through the $S_{h\text{-}Vp}$ iterative calculation (equation (7) and section 4.1).

4.4. Uncertainty Estimation

Throughout the resistivity and velocity calculations to calibrate n, the uncertainty associated with each and every parameter (Table 1 and Figure 5) is tracked at each modeled depth point using a 1,000 trial Monte Carlo approach. At each depth point, each parameter is assigned 1,000 values, centered on the parameter's measured or calculated value and spanning a range from $-b$ to b that accounts for the parameter's uncertainty. A uniform probability distribution function (PDF) is assumed, so the uncertainty in the PDF, δ_{PDF}, is given by $\delta_{\text{PDF}} = b/\sqrt{3}$ (Farrance & Frenkel, 2014). Thus, for the uncertainty of any given variable, δ_{var} (Table 1),

the Monte Carlo simulation assigns a range of values given by $b = \pm \delta_{var} \cdot \sqrt{3}$ and centered around the parameter's measured value. Following the Monte Carlo simulation, the resulting values for n are reported as the mean and standard deviation of the entire matrix of 1,000 values at each depth point.

5. Results

The initial calibration of n is carried out using the extensive, detailed measurements made at the Mallik 2002 Gas Hydrate Production Research Well, Mallik 5L-38, on the Mackenzie Delta in the Northwest Territories, Canada. Additional estimates for n are calculated for hydrate-bearing coarse-grained units in two marine sites from the northern Gulf of Mexico, where hydrate was inferred from logging-while-drilling (LWD) data (Figure 1).

5.1. Mallik

Of the three hydrate sites chosen for this study, the Mallik 5L-38 data set has the most complete set of well logs and detailed core measurements for providing a robust means of estimating n and its uncertainty. We find $n = 2.58 \pm 0.45$ for the Mallik 5L-38 hydrate-bearing sands. The parameters used in this study, and their associated uncertainties at Mallik, are listed in Table 1. Figure 6 plots $S_{h\text{-}Vp}$ and the associated uncertainty in $S_{h\text{-}Vp}$, along with the resistivity-based hydrate saturation, $S_{h-\mathscr{R}}$ for $n = 2.0$, 2.5 and 3.0.

Figure 6 also demonstrates the practical limitations lithology imposes on using resistivity and V_p to estimate hydrate saturation. Some intervals, highlighted in shades of gray, are excluded from the n calibration because of the high likelihood these intervals are not dominated by quartz sand. The gamma ray (Figure 6a) and the photoelectric factor logs (PEF, Figure 6b) are used to evaluate the lithology. Quartz sand generally has a qualitatively low gamma ray value, which is about 50–70 API in the Mallik 5L-38 well. Additionally, the PEF log is sensitive to the average atomic number of the formation, and values of ~2 indicate quartz sand. Intervals outside those ranges are excluded. For example, based on the coal beds found in the cores (Medioli et al., 2005) and the low PEF value of ~1 (which indicates coal) from 1,079 to 1,080.5 m, this interval was excluded from the n calculations. PEF trends higher than 2 indicate an increase in clay or carbonate cementation, and those intervals were also excluded. Finally, values of $S_{h\text{-}Vp}$ below 0.4 (vertical line in Figure 6f) are excluded because this is the threshold below which hydrates can more easily exist in a pore-filling, rather than load-bearing morphology (Lee et al., 2010; Yun et al., 2005).

5.2. Gulf of Mexico

The Gulf of Mexico Gas Hydrate Joint Industry Project drilled and collected LWD data at several locations on the continental slope in the northern Gulf of Mexico during Leg 2 in 2009 (Boswell et al., 2012; Collett et al., 2012). At two sites, thick coarse-grained units were encountered that had markedly increased measured resistivity and compressional velocity in intervals with low gamma ray values, indicating high saturation gas hydrate in sand (Boswell et al., 2012). This study focuses on two wells that penetrated these coarse-grained layers: Walker Ridge Hole 313-H (WR313-H) in the Terrebonne Basin and Green Canyon Hole 955-H (GC955-H) located just off the edge of eastern edge of the Sigsbee escarpment (Figure 1).

In both wells, log measurements were collected using the sonicVISION (denotes mark of Schlumberger) for V_p and the geoVISION (denotes mark of Schlumberger) and EcoScope (denotes mark of Schlumberger) tools for resistivity (Collett et al., 2012). As with Mallik, the resistivity measurement that most closely investigates the same sediment volume as the V_p measurement is selected. The sonicVISION (denotes mark of Schlumberger) V_p measurement has a vertical resolution of ~60 cm and a depth of investigation of ~10 cm. The resistivity log with the closest measured volume is the P16H, which has a vertical resolution of 30–60 cm and a depth of investigation of between 30 and 45 cm, depending on the formation resistivity (Collett et al., 2012). The depth of investigation of the P16H measurement is significantly larger than the V_p measurement in these cases, but there are no significant lateral changes in the environment as the P28H, P32H, and P40H logs, which all have deeper depths of investigation ranging as far as 90 cm, were the same as the P16H resistivity log in both Gulf of Mexico holes. Thus, differing depths of investigation for V_p and P16H the measurements are not a problem in these two cases.

During Joint Industry Project Leg 2, no NMR logs or cores were collected. As LWD is increasingly used for initial characterization of hydrate systems, it is becoming much more common to determine S_h without core

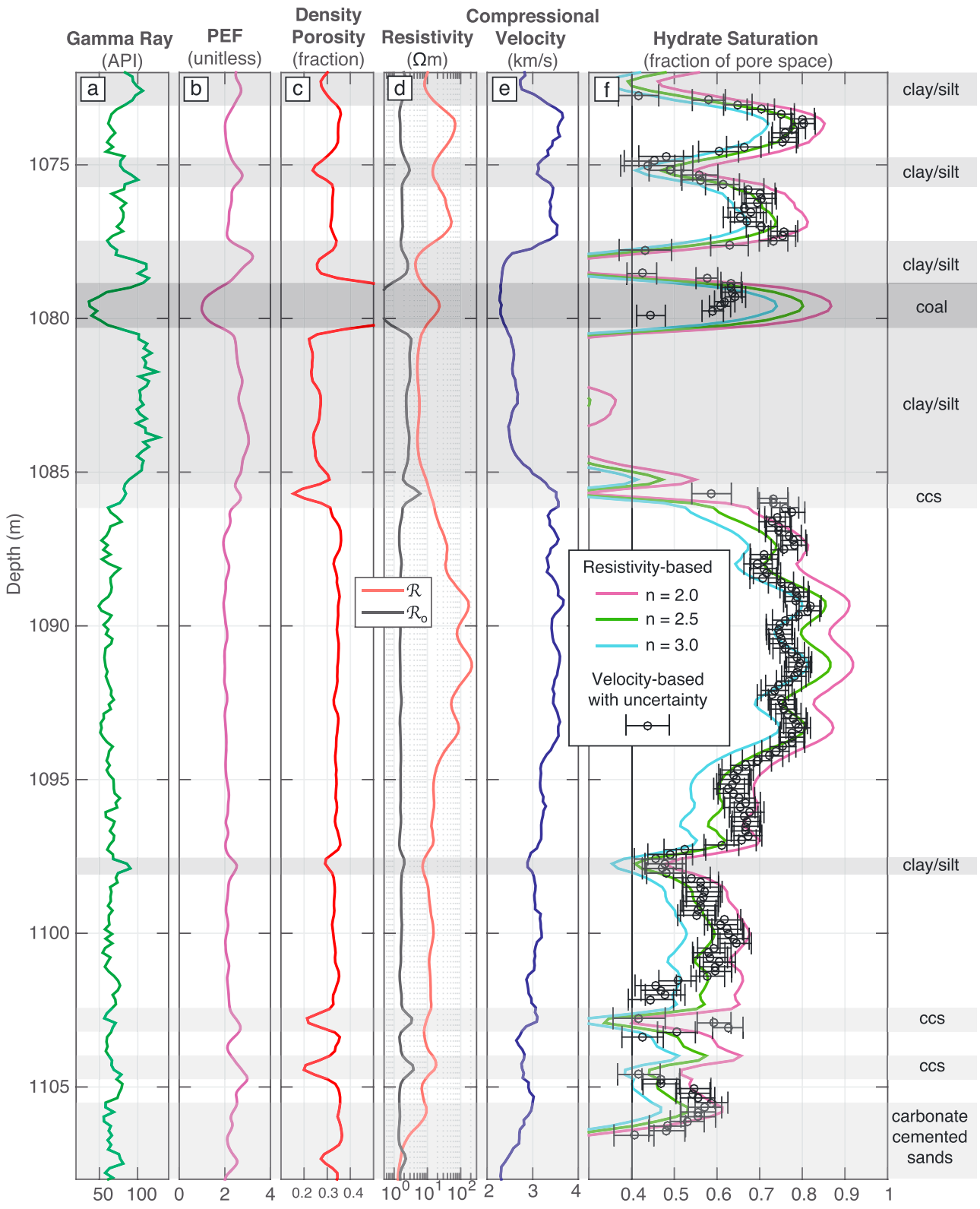

Figure 6. A plot of the well logs, modeled hydrate saturations, identified lithology, and excluded intervals (shaded in gray) for Mallik 5L-38. Tracks a–e display a selection of the measured well logs and the calculated $\mathcal{R}_o$ (equations (2) and (3)). Track f shows the velocity-based gas hydrate calculation, $S_{h\text{-}vp}$, plotted with the resistivity-based gas hydrate saturation, $S_{h\text{-}\rho}$, as calculated using the AHF10 resistivity log with n = 2.0, 2.5, and 3.0. The 0.4 or 40% saturation line is bold because this is the threshold below which hydrates can more easily exist in a pore-filling, rather than load-bearing morphology (Lee et al., 2010; Yun et al., 2005). Carbonate-cemented sands are abbreviated "ccs."

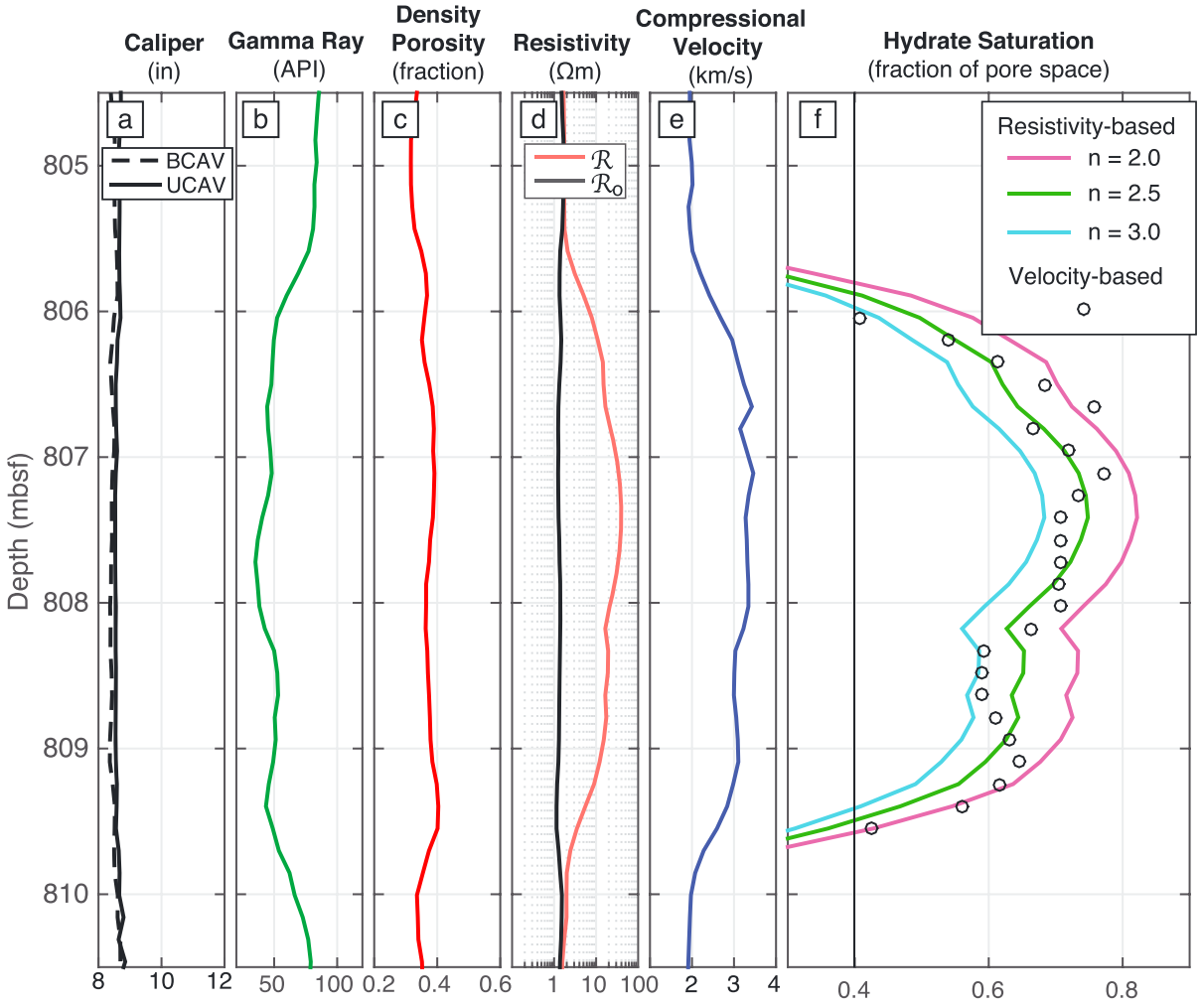

Figure 7. A plot of the well logs, calculated $\mathscr{R}_o$ and model results for Joint Industry Project Leg 2 Hole WR313-H. Track a indicates an in-gauge borehole throughout the sand interval, as defined by low values (< 50 API) on the gamma ray log in Track b. Tracks c–e display measured logs and the calculated $\mathscr{R}_o$ (equations (2) and (3)) used in the model. Track f shows the $S_{h\text{-}Vp}$ (dots) plotted with $S_{h\text{-}\rho}$ as calculated using the P16H resistivity log and n = 2.0, 2.5 and 3.0. The 0.4 or 40% saturation line is bold, because $S_{h\text{-}Vp}$ below this threshold are excluded.

(e.g., Boswell et al., 2012; Kumar et al., 2016). In May 2017, however, the University of Texas (Expedition UT-GOM2-01) collected pressure cores from the reservoir near GC955-H, revealing that the main reservoir was comprised of coarse silt and that hydrate formed in the primary pore space (Flemings et al., 2018). While the silt is composed almost completely of quartz, there were several centimeter to millimeter thick, high-porosity, water-saturated clay layers interbedded within the main silt reservoir. These layers are below the resolution of the available logging data but could contribute an increased conductivity to the bulk resistivity measurements. Erickson and Jarrard (1998) showed, however, that for high-porosity clay (the clay has a $\phi \approx 0.4$), clay conduction is a minor effect. There is no mechanism to remove these thin layer effects from the data as they are below the resolution of the logging tools.

At WR313-H, no core has been collected, so direct measurements proving surface conductivity is negligible cannot be made (Revil et al., 2014). However, the pore water is most likely close to the conductivity of sea-water and the temperature of the system is low ($T < 25$°C), two conditions that make significant surface conductivity contributions less likely. Similarly, centimeter-scale clay interbeds may also exist at WR313-H within the main reservoir (Cook et al., 2012); however, these interbeds would likely have a high porosity similar to GC955-H.

At both Gulf of Mexico locations the standard grain density for quartz sand ρ_g = 2.65 g/cm^3, a pore water salinity of standard seawater, 35 ppt, an assumed seafloor temperature of 4°C, and an estimated geothermal

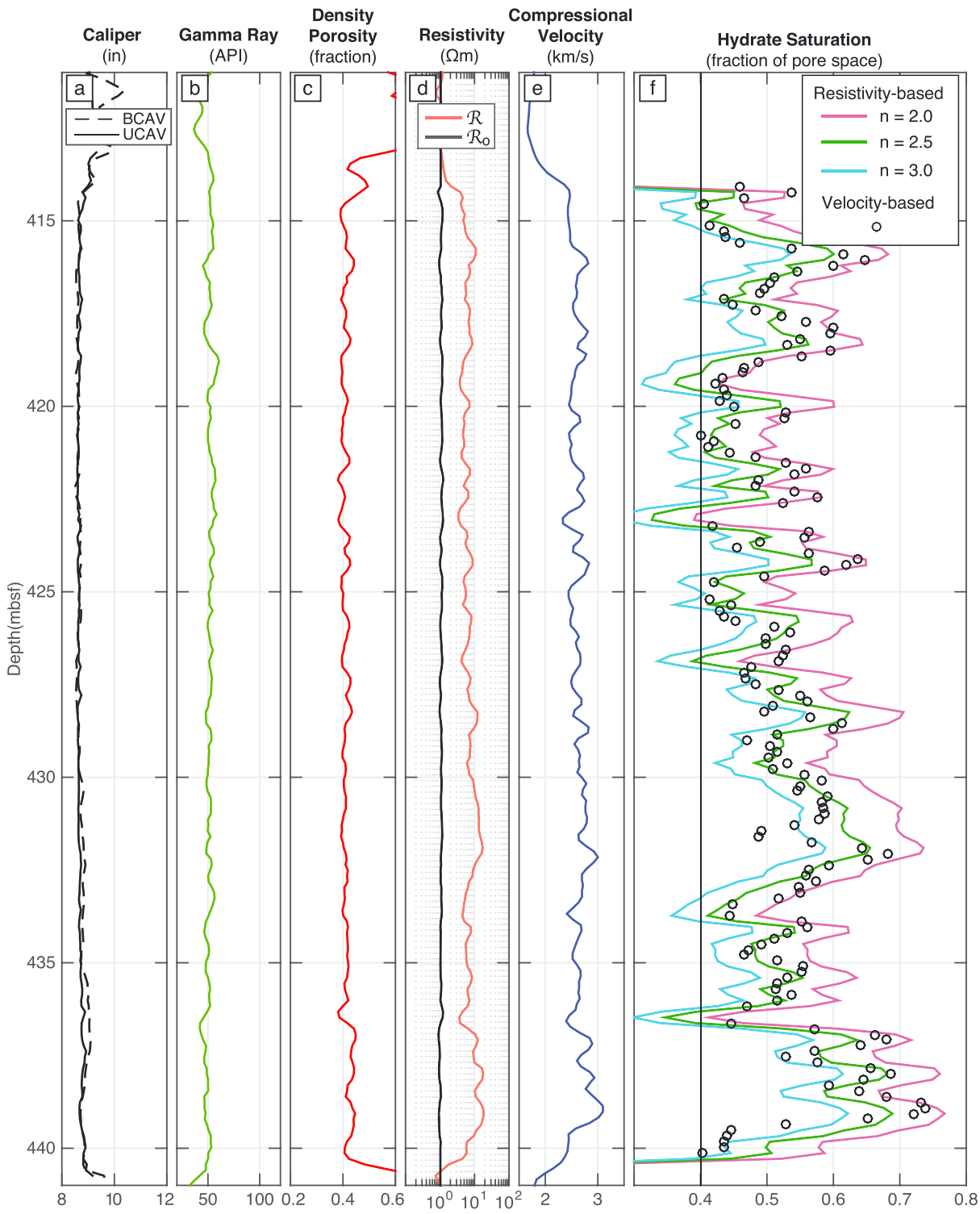

Figure 8. A plot of the well logs, calculated $\mathscr{R}_o$ and model results for Joint Industry Project Leg 2 Hole GC955-H. Track a caliper log indicates an in-gauge borehole within the gas hydrate filled sand, but washed out intervals above and below the gas hydrate filled sand. Tracks c–e contain critical logs and the calculated $\mathscr{R}_o$ (equations (2) and (3)) used in the model. Track f shows the $S_{h\text{-}Vp}$ plotted with the $S_{h\text{-}\rho}$ using the P16H resistivity log and n = 2.0, 2.5, and 3.0. The 0.4 or 40% saturation line is bold, because velocity-based saturations below this threshold are excluded.

Table 2
Archie's Saturation Exponent (n) as Calculated for Each Location in This Study and From Malinverno et al. (2008)

Well name	Archie's saturation exponent
Mallik Hole 5 L-38	$n = 2.58 \pm 0.45$
JIP 2 Hole WR313-H	$n = 2.39$
JIP 2 Hole GC955-H	$n = 2.40$
IODP 311 U1325[a]	$n = 2.42 \pm 0.28$

Note. Recommended value (this study): $n = 2.5 \pm 0.5$. JIP = Joint Industry Project.
[a]From Malinverno et al. (2008).

gradient of 19.5°C/km for Walker Ridge (Frye et al., 2012; McConnell & Kendall, 2002) and 32°C/km for GC955-H (McConnell et al., 2010) are used. The estimated salinity and temperature gradient as well as an assumed hydrostatic pressure gradient are used to calculate R_w using Fofonoff and Millard (1983). In both holes, m is set to 1.8, calibrated on a 20 m sandy interval in Hole WR313-G (Cook et al., 2010). We do not track uncertainty at these sites in our calculations because key data such as temperature (GC955-H and WR313-H) or grain size (WR313-H) are not available. Furthermore, we know about the occurrence of centimeter-millimeter thick clay interbeds at GC955-H, but we have no mechanism to remove them from our model due to the resolution of our data.

At WR313-H, the analysis focuses on the upper section of the Orange sand unit, from 806 to 810 mbsf (meters below seafloor), which is well defined by the reduction in gamma ray values (Figure 7b). The hole is in gauge throughout that section (bit size is 8 ¾ in or 22 cm, Figure 7a), producing high-quality log data. There is also a lower section of the Orange Sand, from 812 to 818 mbsf, but the section is not included in the final analysis of n due to its very low measured resistivity and enlarged borehole diameter, which can degrade the quality of the measured logs.

The measured logs and the results of the n calibration for WR313-H are plotted in Figure 7. Almost all of the velocity-based gas hydrate saturations plot within the range of $n = 2.0$ to 3.0, with the mean n value of 2.39.

At GC955-H, a thick coarse-grained unit was encountered from 385 to 488 mbsf, yet only an interval from 414 to 440 mbsf and a few thin layers below 440 mbsf contained gas hydrate (Figure 8). The silt surrounding the hydrate saturated interval was water-saturated and unlithified, resulting in significant borehole washouts that greatly affected the quality of many borehole measurements above and below the gas hydrate filled subintervals. The subintervals containing gas hydrate, however, are in gauge (Figure 8a). Similar to WR313-H, most of the model results fall within $n = 2.0$ to 3.0, with a mean n value of 2.40.

6. Discussion

Within the calibration method presented herein, n values from both marine (WR313-H and GC955-H) and permafrost locations (Mallik 5L-38) are found to be close to $n \approx 2.5$ (Table 2). In conjunction with the value of $n = 2.42 \pm 0.28$ calibrated by Malinverno et al. (2008), these results (Table 2) suggest a potential universality for n in hydrate-bearing sands regardless of environment. If an n value cannot be independently calibrated in a laboratory or by using additional field data as shown herein or in Malinverno et al. (2008), we recommend the use of $n = 2.5 \pm 0.5$ as long as the reservoir is course-grained and the pore water is saline.

6.1. Lithology Considerations

The Mallik 5L-38 hole was chosen for this calibration in part because of the significant body of information associated with the site but also because Mallik contains a well-documented massive sand with only a few interbeds of carbonate cemented sand and silt (Medioli et al., 2005). The nonsand intervals were identifiable from well log and core information and could thus be excluded from the Mallik analysis (Figure 6).

In Gulf of Mexico Holes WR313-H and GC955-H, thin clay beds that are below the resolution of the gamma ray measurement may be the reason $S_{h\text{-}Vp}$ appears more scattered within the n value bounds of $S_{h\text{-}\rho}$ (Figures 7 and 8) than in the Mallik results (Figure 6). Variations in S_h within the reservoir may also contribute to some of the scatter (Cook et al., 2012). In either case, the variations in lithology or hydrate saturation within the reservoir affect the measured V_p and resistivity differently near the interface of the variation, certainly causing some of the scatter in the overall match.

6.2. Saturation Exponent Variability

For conventional oil and gas reservoirs, n values are determined in laboratory specimens by varying water saturation, S_w, ($S_w = 1 - S_h$) and measuring resistivity at each S_w. The n value is identified using a logarithmic crossplot of the S_w versus the resistivity index ($R/\mathscr{R}_o$). Though n is often reported as simply a single value, n

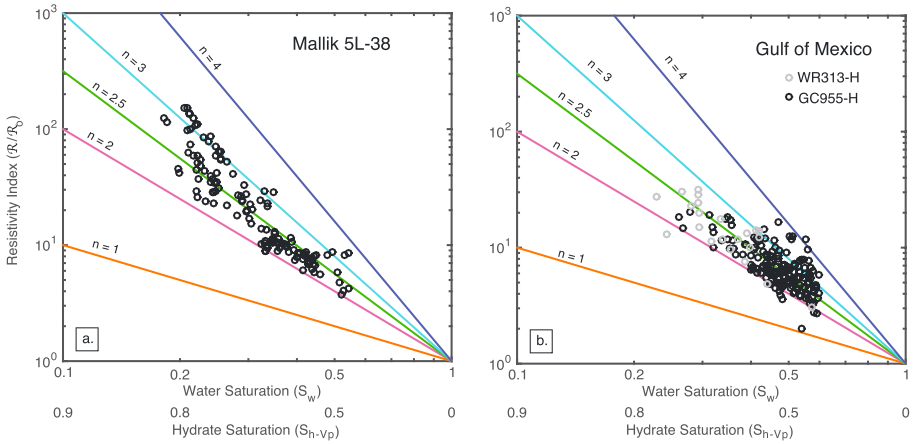

Figure 9. Crossplots of water saturation (S_w) versus resistivity index for (a) Mallik 5L-38 and (b) Gulf of Mexico Holes WR313-H and GC955-H.

values are rarely, if ever, exclusively single valued. Finding n value ranges is typical in oil and gas reservoir applications (Anderson, 1986; Ellis & Singer, 2007; Kumar et al., 2011; Sweeney & Jennings, 1960).

Figure 9 shows an $S_{w\text{-}Vp}$ versus resistivity index crossplot, displaying data from Mallik 5L-38 and the two Gulf of Mexico wells. For Mallik, n varies slightly as hydrate saturations change (Figure 9a). At midrange hydrate saturations from 0.55 to 0.65, n values cluster lower, near n = 2.3 and 2.4, and nearly all below n = 2.5. At saturations greater than 0.65 or lower than 0.55, there is a wider range in n values, and less clustering. At the very highest saturations, greater than 0.75, n values trend slightly higher, to n = 3. It should be noted that if surface conductivity of the sediment grains affected n, a reduction in the value of n as hydrate saturation increased should be apparent, yet the opposite trend is observed in Figure 9a. In Figure 9b, The n values do not appear to have any clear trend with saturation for Holes WR313-H or GC955-H.

The value calibrated here for n, 2.5 ± 0.5, is slightly higher than the common value ($n \approx 2$) for water-wet oil and natural gas reservoirs (Ellis & Singer, 2007), or for ice ($n \approx 1.9$) (Pearson et al., 1983). A situation where higher n values were found that is directly applicable to high-porosity, marine and permafrost sand reservoirs is discussed in Kumar et al. (2011). Kumar et al. (2011) produced numerical models from microcomputed tomography images of rocks and sediments to constrain Archie's saturation exponent. A model for high porosity sands (ϕ = 0.34) found $n \approx 2.41$. The authors hypothesize that the n value is higher than the more common value, $n \approx 2$, because there are fewer grain contacts observed in the ϕ = 0.34 sand than is typical for lower porosity, conventional sandstone reservoirs. This model further supports n values found here for Mallik and the Gulf of Mexico (Table 2), all of which have a similarly high porosity of $\phi > 0.3$; high porosity is common in hydrate reservoirs, suggesting it may be important to consider both porosity and grain contacts in future resistivity-based investigations of sand reservoirs.

While the $S_{h\text{-}Vp}$ component of our model is limited to $S_{h\text{-}Vp} > 0.4$, there will likely be cases where n is unknown in reservoirs with low resistivity and effectively, $S_h < 0.4$. In these cases, we recommend the cautious use of $n = 2.5 \pm 0.5$, as the trend developed at $S_h > 0.4$ (Figure 9) is likely applicable at lower hydrate saturations in sand reservoirs. Our approach cannot address the validity at $S_h < 0.4$ because the influence of hydrate on the measured V_p becomes relatively weak below the 0.4 threshold (Yun et al., 2005); however, the influence of hydrate on the measured resistivity most likely follows Archie's equation (equation (4)) below the 0.4 threshold.

Finally, it should be noted that some reservoirs may contain lower S_h due to reservoir characteristics such as the presence of significant clay concentrations, and this model may not be applicable. Use of $n = 2.5 \pm 0.5$ can only be recommended for resistivity measurements in coarse-grained reservoirs where hydrate forms in the primary pore space.

7. Conclusions

Archie's equation is routinely applied to resistivity well logs to determine natural gas hydrate saturation, S_h. We calibrate the saturation exponent, n, an empirical parameter in Archie's equation for gas hydrate-bearing

sand reservoirs using independent S_h determined from applying a load-bearing model to compressional-wave velocity well log data. For the permafrost Mallik site and the marine Gulf of Mexico sites, using $n = 2.5 \pm 0.5$ yields the closest agreement between electrical resistivity and compressional-wave velocity predictions of S_h.

When possible, n should be calibrated using site specific and reservoir specific data, but for coarse-grained reservoirs in brine-saturated environments where n is not calibrated, the use of $n = 2.5 \pm 0.5$ is recommended.

Appendix A: Surface Conductivity of the Mallik Sand

An electrical double layer occurs even in clean sands, meaning that surface conductivity along sand grains can contribute to the measured bulk electrical conductivity (e.g., Revil et al., 2014; Rink & Schopper, 1974; Wildenschild et al., 2000). This appendix shows why, for the Mallik 5L-38 sand represented in Figures 2, 4, and 6, surface conductivity is negligible.

The Mallik sand is well sorted and does not have significant fine-grained material (Uchida et al., 2005). It is composed chiefly of quartz, with a grain density of 2.66 gm/cm^3. (Table 1) (Winters et al., 2005). As noted in Revil et al. (2014, p. D311) surface conductivity in well-sorted sands can be neglected in equation (1) and in subsequent Archie saturation calculations when the pore water conductivity, σ_w, is significantly greater than the intrinsic surface conductivity, σ_s, even as water saturation (S_w) in the pore space, ϕ, decreases. This condition is expressed as

$$\sigma_w \gg \frac{F\sigma_s}{S_w} \text{ where } F = \frac{1}{\phi^m}. \tag{A1}$$

These calculations use the mean porosity, $\phi = 0.33$, of the subselected Mallik sand in Figure 6, which is corrected for hydrate saturation in equation (7). The value used for m, $m = 1.7$, is calculated in section 4.2. The intrinsic surface conductivity, as defined by Revil et al. (2014), is

$$\frac{\sigma_s = 6Q_S\beta_{(+)}}{d} \tag{A2}$$

where Qs is the equivalent charge density on the mineral surface, $\beta_{(+)}$ is the mobility of the cation, and d is the mean grain diameter (if the sand is well sorted). Here we use the charge density suggested by Revil (2013) and Revil et al. (2014) for a well-sorted quartz sand, $Q_s = 0.64$ C/m^2. At Mallik, the pore water is dominated by sodium chloride (Kulenkampff & Spangenberg, 2005), so the primary cation is Na^+. With equation (A3), we adjust the value of $\beta_{(+)}$ for the ~12°C temperature (T) of the Mallik sand in the interval of interest using the relation from Revil et al. (1998):

$$\beta_{(+)}(T) = \beta_{(+)}(T_o)(1 + \alpha(T - T_o)). \tag{A3}$$

The parameter α describes the relationship between Na^+ mobility and temperature. For low temperatures ($T < 25$°C), α is about 0.02/°C (Hayley et al., 2007). Using the value for Na^+ mobility at 25°C, $\beta_{(+)} = 5.0 \times 10^{-8}$ m^2/sV (Koneshan et al., 1998), the adjusted mobility of Na^+ at 12°C is $\beta_{(+)} = 3.7 \times 10^{-8}$ m^2/sV. Finally, the Mallik sand is a well sorted, fine- to medium-grained sand with a mean grain size of ~260 μm (Medioli et al., 2005), used here as the parameter d in equation (A2).

The pore water conductivity in the Mallik sand is $\sigma_w = 4.0$ S/m (Table 1, $\sigma_w = 1/\rho_w$). This pore water conductivity is significantly greater than $\sigma_s / S_w\phi$, which ranges from 0.019 S/m at $S_w = 0.18$ (the lowest water saturation, as determined by V_p modeling) to 0.006 S/m at $S_w = 0.6$ (the highest S_w, defined by the cutoff of S_h at 0.4 due to the V_p model's hydrate sensitivity (Yun et al., 2007). This means the relationship shown in equation (A1) is satisfied, implying that surface conductivity is negligible. This result is further supported by the crossplot of our results in Figure 9a. If surface conductivity was nonnegligible, n should reduce as S_h increases, creating a concave downwards shape. The opposite trend occurs at Mallik (Figure 9a).

In many hydrate-bearing sand reservoirs, surface conductivity is likely negligible, since most environments have a high pore water conductivity similar to seawater, high porosity ($\phi > 0.3$), and low temperature ($T < 25$°C). Reservoirs in freshwater hydrate environments such as Lake Baikal in Russia (e.g., Van Rensbergen et al., 2002), however, most likely have a significant surface conductivity contribution.

Additionally, the surface conductivity should be accounted for in sand reservoirs containing clay particles, using models such as Revil (2013).

Disclaimer

This report was prepared as an account of work sponsored by an agency of the United States Government. Neither the United States Government nor any agency thereof, nor any of their employees, makes any warranty, express or implied, or assumes any legal liability or responsibility for the accuracy, completeness, or usefulness of any information, apparatus, product, or process disclosed, or represents that its use would not infringe privately owned rights. Reference herein to any specific commercial product, process, or service by trade name, trademark, manufacturer, or otherwise does not necessarily constitute or imply its endorsement, recommendation, or favoring by the United States Government or any agency thereof. The views and opinions of authors expressed herein do not necessarily state or reflect those of the United States Government or any agency thereof.

Acknowledgments
The authors thank the planners, scientists, and personnel associated with the Mallik and JIP Leg 2 projects. Data from both of these projects are publically available through the Government of Canada (gescan.nrcan.gc.ca) for the Mallik data and through Lamont-Doherty (brg.ldeo.columbia.edu/ghp/) for the Gulf of Mexico data. This manuscript was strengthened by comments from Erik Spangenberg and several anonymous reviewers. This project was partially funded under DOE award DE-FE0023919 and the Gas Hydrate Project of the U.S. Geological Survey's Coastal and Marine Geology Program. Author A. Cook also acknowledges support from the National Academy of Science Gulf Research Fellowship.

References

Anderson, B. I., Barber, T. D., Luling, M. G., Rasmus, J., Sen, P. N., Tabanou, J. R., & Haugland, M. (2007). Observations of large dielectric effects on LWD propagation-resistivity logs. SPWLA 48th Annual Logging Symposium, BB.

Anderson, W. G. (1986). Wettability literature survey—Part 3: The effects of wettability on the electrical properties of porous media. *Journal of Petroleum Technology*, *38*(12), 1371–1378. https://doi.org/10.2118/13934-PA

Archer, D. (2007). Methane hydrate stability and anthropogenic climate change. *Biogeosciences*, *4*(4), 521–544. https://doi.org/10.5194/bg-4-521-2007

Archie, G. E. (1942). The electrical resistivity log as an aid in determining some reservoir characteristics. *Transactions of the American Institute of Mining and Metallurgical Engineers*, *146*, 54–62.

Batzle, M., & Wang, Z. (1992). Seismic properties of pore fluids. *Geophysics*, *57*(11), 1396–1408. https://doi.org/10.1190/1.1443207

Biastoch, A., Treude, T., Rüpke, L. H., Riebesell, U., Roth, C., Burwicz, E. B., et al. (2011). Rising Arctic Ocean temperatures cause gas hydrate destabilization and ocean acidification. *Geophysical Research Letters*, *38*, L08602. https://doi.org/10.1029/2011GL047222

Boswell, R., & Collett, T. S. (2011). Current perspectives on gas hydrate resources. *Energy & Environmental Science*, *4*(4), 1206–1215. https://doi.org/10.1039/c0ee00203h

Boswell, R., Collett, T. S., Frye, M., Shedd, W., McConnell, D. R., & Shelander, D. (2012). Subsurface gas hydrates in the northern Gulf of Mexico. *Marine and Petroleum Geology*, *34*(1), 4–30. https://doi.org/10.1016/j.marpetgeo.2011.10.003

Chaouachi, M., Falenty, A., Sell, K., Enzmann, F., Kersten, M., Haberthür, D., & Kuhs, W. F. (2015). Microstructural evolution of gas hydrates in sedimentary matrices observed with synchrotron X-ray computed tomographic microscopy. *Geochemistry, Geophysics, Geosystems*, *16*, 1711–1722. https://doi.org/10.1002/2015GC005811

Choi, J., Dai, S., Cha, J., & Seol, Y. (2014). Laboratory formation of noncementing hydrates in sandy sediments. *Geochemistry, Geophysics, Geosystems*, *15*, 1648–1656. https://doi.org/10.1002/2014GC005287

Clavier, C., Heim, A., & Scala, C. (1976). Effects of pyrite on resistivity and other logging measurements. *SPWLA Seventeenth Annu, Logging Symp. 9-12, 1976*, 1–34.

Clennell, M., Ben, M., Josh, L., Esteban, D., Hill, C., Woods, C. D., et al. (2010). The influence of pyrite on rock electrical Properties: A case study from NW Australian gas reservoirs, *SPWLA 51st Annu. Logging Symp.*, 1–13. https://doi.org/10.13140/2.1.4026.0483

Collett, T., Johnson, A., Knapp, C., & Boswell, R. (2009). Natural gas hydrates—A review. In T. Collett, et al. (Eds.), *Natural gas hydrates*, *AAPG Memoir 89* (pp. 146–220). Tulsa, OK: American Association of Petroleum Geologists.

Collett, T. S., Boswell, R., Cochran, J. R., Kumar, P., Lall, M., Mazumdar, A., et al. (2014). Geologic implications of gas hydrates in the offshore of India: Results of the National Gas Hydrate Program Expedition 01. *Marine and Petroleum Geology*, *58*(Part A), 3–28. https://doi.org/10.1016/j.marpetgeo.2014.07.021

Collett, T. S., & Ladd, J. (2000). Detection of gas hydrate with downhole logs and assessment of gas hydrate concentrations (saturations) and gas volumes on the Blake Ridge with electrical resistivity log data. *Proceeding of the Ocean Drilling Program, Scientific Results*, *164*, 179–191.

Collett, T. S., Lee, M. W., Zyrianova, M. V., Mrozewski, S. A., Guerin, G., Cook, A. E., & Goldberg, D. S. (2012). Gulf of Mexico Gas Hydrate Joint Industry Project Leg II logging-while-drilling data acquisition and analysis. *Marine and Petroleum Geology*, *34*(1), 41–61. https://doi.org/10.1016/j.marpetgeo.2011.08.003

Cook, A., Guerin, G., Mrozewski, S., Collett, T., & Boswell, R. (2010). Gulf of Mexico Gas Hydrate Joint Industry Project Leg II: Walker Ridge 313 LWD operations and results. Retrieved from http://www.netl.doe.gov/research/oil-and-gas/methane-hydrates/2009-gom-jip-leg2-reports

Cook, A. E., Anderson, B. I., Rasmus, J., Sun, K., Li, Q., Collett, T. S., & Goldberg, D. S. (2012). Electrical anisotropy of gas hydrate-bearing sand reservoirs in the Gulf of Mexico. *Marine and Petroleum Geology*, *34*(1), 72–84. https://doi.org/10.1016/j.marpetgeo.2011.09.003

Dai, S., Lee, C., & Carlos Santamarina, J. (2011). Formation history and physical properties of sediments from the Mount Elbert Gas Hydrate Stratigraphic Test Well, Alaska North Slope. *Marine and Petroleum Geology*, *28*(2), 427–438. https://doi.org/10.1016/j.marpetgeo.2010.03.005

Dickens, G. R., Castillo, M. M., & Walker, J. C. G. (1997). A blast of gas in the latest Paleocene: Simulating first-order effects of massive dissociation of oceanic methane hydrate. *Geology*, *25*(3), 259–262. https://doi.org/10.1130/0091-7613(1997)025%3C0259:ABOGIT%3E2.3.CO;2

Dickens, G. R., Paull, C. K., & Wallace, P. (1997). Direct measurement of in situ methane quantities in a large gas-hydrate reservoir. *Nature*, *385*(6615), 426–428. https://doi.org/10.1038/385426a0

Du Frane, W. L., Stern, L. A., Weitemeyer, K. A., Constable, S., Pinkston, J. C., & Roberts, J. J. (2011). Electrical properties of polycrystalline methane hydrate. *Geophysical Research Letters*, *38*, L09313. https://doi.org/10.1029/2011GL047243

Dvorkin, J., & Nur, A. (1996). Elasticity of high-porosity sandstones: Theory for two North Sea data sets. *Geophysics*, *61*(5), 1363–1370. https://doi.org/10.1190/1.1444059

Dvorkin, J., Prasad, M., Sakai, A., & Lavoie, D. (1999). Elasticity of marine sediments: Rock physics modeling. *Geophysical Research Letters*, *26*(12), 1781–1784. https://doi.org/10.1029/1999GL900332

Dvorkin, J. M., Helgerud, B., Waite, W. F., Kirby, S. H., & Nur, A. (2000). Introduction to physical properties and elasticity models. In M. D. Max (Ed.), *Natural gas hydrate in oceanic and permafrost environment* (pp. 245–260). Dordrecht, Netherlands: Kluwer Academic.

Ebinuma, T., Kanata, Y., Minagawa, H., Ohmura, R., Nagao, J., & Marita, H. (2005). Mechanical properties of sandy sediment containing methane hydrate, paper 3037, Fifth International Conference on Gas Hydrates, Trondheim, Norway. 12–16 June.

Ellis, D. V., & Singer, J. M. (2007). *Well logging for Earth scientists* (2nd ed.). Netherlands: Springer. https://doi.org/10.1007/978-1-4020-4602-5

Erickson, S. N., & Jarrard, R. D. (1998). Porosity/formation-factor relationships for high-porosity siliciclastic sediments from Amazon Fan. *Geophysical Research Letters*, *25*(13), 2309–2312. https://doi.org/10.1029/98GL01777

Farrance, I., & Frenkel, R. (2014). Uncertainty in measurement: A review of Monte Carlo simulation using Microsoft Excel for the calculation of uncertainties through functional relationships, including uncertainties in empirically derived constants. *Clinical Biochemist Reviews*, *35*(1), 37–61.

Flemings, P. B., Phillips, S. C., Collett, T. S., Cook, A. E., Boswell, R., & the UT-GOM2 Expedition Scientists (2018). UT-GOM2-1 hydrate pressure coring expedition report. University of Texas at Austin.

Fofonoff, N. P., & Millard, R. C. (1983). *Algorithms for computation of fundamental properties of seawater* (53 pp.). UNESCO.

Frye, M., Shedd, W., & Boswell, R. (2012). Gas hydrate resource potential in the Terrebonne Basin, Northern Gulf of Mexico. *Marine and Petroleum Geology*, *34*(1), 150–168. https://doi.org/10.1016/j.marpetgeo.2011.08.001

Gassmann, F. (1951). Uber die elastizitat poroser medien. *Vierteljahrsschrift der Naturforschenden Gesellschaft in Zürich*, *96*, 1–23.

Goldberg, D. S., Kleinberg, R. L., Weinberger, J. L., Malinverno, A., McLellan, P. J., & Collett, T. S. (2010). Evaluation of natural gas-hydrate systems using borehole logs. *Geophysical Characterization of Gas Hydrates*, 239–262. https://doi.org/10.1190/1.9781560802197.ch16

Hayley, K., Bentley, L. R., Gharibi, M., & Nightingale, M. (2007). Low temperature dependence of electrical resistivity: Implications for near surface geophysical monitoring. *Geophysical Research Letters*, *34*, L18402. https://doi.org/10.1029/2007GL031124

Helgerud, M. B., Waite, W. F., Kirby, S. H., & Nur, A. (2009). Elastic wave speeds and moduli in polycrystalline ice Ih, sI methane hydrate, and sII methane-ethane hydrate. *Journal of Geophysical Research*, *114*, B02212. https://doi.org/10.1029/2008JB006132

Henninges, J., Schotter, J., Erbas, K., & Huenges, E. (2005). Temperature field of the Mallik gas hydrate occurence—Implications on phase changes and thermal properties. In S. R. Dallimore & T. S. Collett (Eds.), *Scientific results from the Mallik 2002 Gas Hydrate Production Research Well Program, MacKenzie Delta*, *Bulletin No. 585* (p. 14). Northwest Territories, Canada: Geological Survey of Canada.

Hill, R. (1952). The elastic behavior of crystalline aggregate. *Proceedings of the Physical Society of London*, *A65*, 349–354.

Holland, M., & Schultheiss, P. (2014). Comparison of methane mass balance and X-ray computed tomographic methods for calculation of gas hydrate content of pressure cores. *Marine and Petroleum Geology*, *58*, 168–177. https://doi.org/10.1016/j.marpetgeo.2014.07.016

Jackson, P., Smith, D., & Stanford, P. (1978). Resistivity-porosity-particle shape relationships for marine sands. *Geophysics*, *43*(6), 1250–1268. https://doi.org/10.1190/1.1440891

Johnson, A. H. (2011). Global resource potential of gas hydrate—A new calculation, *Proceedings of the 7th International Conference on Gas Hydrates*. Edinburgh, Scotland, UK.

Kerkar, P. B., Horvat, K., Jones, K. W., & Mahajan, D. (2014). Imaging methane hydrates growth dynamics in porous media using synchrotron X-ray computed microtomography. *Geochemistry, Geophysics, Geosystems*, *15*, 4759–4768. https://doi.org/10.1002/2014GC005373

Kleinberg, R. L., Flaum, C., & Collett, T. S. (2005). Magnetic resonance log of JAPEX/JNOC/GSC et al. Mallik 5L-38 gas hydrate production research well: Gas hydrate saturation, growth habit and relative permeability. In S. R. Dallimore & T. S. Collett (Eds.), *Scientific results from the Mallik 2002 as Hydrate Production Research Well Program, Makenzie Delta*, *Bulletin no. 585* (p. 10). Northwest Territories, Canada: Geological Survey of Canada.

Knight, R. J., & Nur, A. (1987). The dielectric constant of sandstones, 60 kHz to 4 MHz. *Geophysics*, *52*(5), 644–654. https://doi.org/10.1190/1.1442332

Koneshan, S., Rasaiah, J. C., Lynden-Bell, R., & Lee, S. (1998). Solvent structure, dynamics, and ion mobility in aqueous solutions at 25°C. *The Journal of Physical Chemistry B*, *102*(21), 4193–4204. https://doi.org/10.1021/jp980642x

Konno, Y., Jin, Y., Yoneda, J., Kida, M., Egawa, K., Ito, T., et al. (2015). Effect of methane hydrate morphology on compressional-wave velocity of sandy sediments: Analysis of pressure cores obtained in the Eastern Nankai Trough. *Marine and Petroleum Geology*, *66*(2), 425–433. https://doi.org/10.1016/j.marpetgeo.2015.02.021

Kulenkampff, J., & Spangenberg, E. (2005). Physical properties of cores from the JAPEX/JNOC/GSC et al. Mallik 5L-38 Gas Hydrate Proudction Research Well under simulated in situ conditions using the Field Laboratory Experimental Core Analysis System (FLECAS*)*. In S. R. Dallimore & T. S. Collett (Eds.), *Scientific results from the Mallik 2002 Gas Hydrate Production Research Well Program, MacKenzie Delta*, *Bulletin No. 585* (p. 16). Northwest Territories, Canada: Geological Survey of Canada.

Kumar, M., Senden, T. J., Sheppard, A. P., Arns, C. H., & Kackstedt, M. A. (2011). Probing the Archie's exponent under variable saturation conditions. *Petrophysics*, *52*, 124–134.

Kumar, P., Collett, T. S., Vishwanath, K., Shukla, K. M., Nagalingam, J., Lall, M. V., et al. (2016). Gas hydrate-bearing sand reservoir systems in the offshore of India: Results of the India National Gas Hydrate Program Expedition 02. *Fire and Ice*, *16*, 1–8.

Lee, J. Y., Francisca, F. M., Santamarina, J. C., & Ruppel, C. (2010). Parametric study of the physical properties of hydrate-bearing sand, silt, and clay sediments: 2. Small-strain mechanical properties. *Journal of Geophysical Research*, *115*, B11105. https://doi.org/10.1029/2009JB006670

Lee, J. Y., Jung, J. W., Lee, M. H., Bahk, J. J., Choi, J., Ryu, B. J., & Schultheiss, P. (2013). Pressure core based study of gas hydrates in the Ulleung Basin and implication for geomechanical controls on gas hydrate occurrence. *Marine and Petroleum Geology*, *47*, 85–98. https://doi.org/10.1016/j.marpetgeo.2013.05.021

Lee, M. W., & Collett, T. S. (2011). In-situ gas hydrate hydrate saturation estimated from various well logs at the Mount Elbert Gas Hydrate Stratigraphic Test Well, Alaska North Slope. *Marine and Petroleum Geology*, *28*(2), 439–449. https://doi.org/10.1016/j.marpetgeo.2009.06.007

Lu, H., Dutrisac, R., Ripmeeser, J., Wright, F., & Uchida, T. (2005). Measurements of gas hydrate saturation in sediment cores recovered from the JAPEX/JNOC/GSC et al. Mallik 5L-38 gas hydrate production research well. In S. R. Dallimore & T. S. Collett (Eds.), *Scientific results from the Mallik 2002 Gas Hydrate Production Research Well Program, Mackenzie Delta*, *Bulletin no. 585* (p. 8). Northwest Territories, Canada: Geological Survey of Canada.

Malinverno, A., Kastner, M., Torres, M. E., & Wortmann, U. G. (2008). Gas hydrate occurrence from pore water chlorinity and downhole logs in a transect across the northern Cascadia margin (Integrated Ocean Drilling Program Expedition 311). *Journal of Geophysical Research*, *113*, B08103. https://doi.org/10.1029/2008JB005702

McConnell, D., Boswell, R., Collett, T., Frye, M., Shedd, W., Guerin, G., et al. (2010). Gulf of Mexico Gas Hydrate Joint Industry Project Leg II: Green Canyon 955 site summary. Retrieved from http://www.netl.doe.gov/research/oil-and-gas/methane-hydrates/2009-gom-jip

McConnell, D. R., & Kendall, B. A. (2002). Images of the base of gas hydrate stability, northwest Walker Ridge, Gulf of Mexico. Houston, TX: Offshore Technology Conference.

Medioli, B. E., Wilson, N., Dallimore, S. R., Pare, D., Brennan-Alpert, P., & Oda, H. (2005). Sedimentology of the cored interval, JAPEX/JNOC/GSC et al. Mallik 5L-38 gas hydrate production research well. In S. R. Dallimore & T. S. Collett (Eds.), *Scientific results from the Mallik 2002 Gas Hydrate Production Research Well Program, MacKenzie Delta*, *Bulletin No. 585* (p. 21). Northwest Territories, Canada: Geological Survey of Canada.

Mindlin, R. D. (1949). Compliance of elastic bodies in contact. *Journal of Applied Mechanics*, *16*, 259–268.

Nur, A., Mavko, G., Dvorkin, J., & Galmudi, D. (1998). Critical porosity: A key to relating physical properties to porosity in rocks. *The Leading Edge*, *17*(3), 357–362. https://doi.org/10.1190/1.1437977

Pabst, W., & Gregorova, E. (2013). Elastic properties of silica polymorphs—A review. *Ceramica-Silikáti*, *57*, 167–184.

Pearson, C. F., Halleck, P. M., McGuire, P. L., Hermes, R., & Mathews, M. (1983). Natural gas hydrate deposits: A review of in situ properties. *Journal of Physical Chemistry*, *87*(21), 4180–4185. https://doi.org/10.1021/j100244a041

Priest, J. A., Best, A. I., & Clayton, C. R. I. (2005). A laboratory investigation into the seismic velocities of methane gas hydrate-bearing sand. *Journal of Geophysical Research*, *110*, B04102. https://doi.org/10.1029/2004JB003259

Priest, J. A., Rees, E. V. L., & Clayton, C. R. I. (2009). Influence of gas hydrate morphology on the seismic velocities of sands. *Journal of Geophysical Research*, *114*, B11205. https://doi.org/10.1029/2009JB006284

Revil, A. (2013). Effective conductivity and permittivity of unsaturated porous materials in the frequency range 1 mHz–1GHz. *Water Resources Research*, *49*, 306–327. https://doi.org/10.1029/2012WR012700

Revil, A., Cathles, L. M., Losh, S., & Nunn, J. A. (1998). Electrical conductivity in shaly sands with geophysical applications. *Journal of Geophysical Research*, *103*, 23,925–23,936. https://doi.org/10.1029/98JB02125

Revil, A., Kessouri, P., & Torres-Verdín, C. (2014). Electrical conductivity, induced polarization, and permeability of the Fontainebleau sandstone. *Geophysics*, *79*(5), D301–D318. https://doi.org/10.1190/geo2014-0036.1

Rink, M., & Schopper, J. R. (1974). *Interface conductivity and its implications to electric logging*. Paper presented at the 15th Annual Logging Symposium.

Ruppel, C., & Kessler, J. D. (2017). The interaction of climate change and methane hydrates. *Reviews of Geophysics*, *55*, 126–168. https://doi.org/10.1002/2016RG000534

Ryu, B., Collett, T. S., Riedel, M., Kim, G. Y., Chun, J., Bahk, J., et al. (2013). Scientific results of the Second Gas Hydrate Drilling Expedition in the Ulleung Basin (UBGH2). *Marine and Petroleum Geology*, *47*, 1–20. https://doi.org/10.1016/j.marpetgeo.2013.07.007

Santamarina, J. C., Dai, S., Terzariol, M., Jang, J., Waite, W. F., Winters, W. J., et al. (2015). Hydro-bio-geomechanical properties of hydrate-bearing sediments from Nankai Trough. *Marine and Petroleum Geology*, *66*(2), 434–450. https://doi.org/10.1016/j.marpetgeo.2015.02.033

Santamarina, J. C., & Ruppel, C. (2008). The impact of hydrate saturation on the mechanical, electrical, and thermal properties of hydrate-bearing sand, silts, and clay. In P. Englezos & J. Ripmeester (Eds.), *Proceedings of the 6th International Conference on Gas Hydrates*. Vancouver, Canada.

Schlumberger (2004). AIT array induction imager tools. Retrieved from http://www.slb.com

Schlumberger (2009). Multi express: Slim, multiconveyance formation evaluation platform. Retrieved from http://www.slb.com

Schlumberger (2014). DSI dipole shear sonic imager. Retrieved from http://www.slb.com

Schwalenberg, K., Haeckel, M., Poort, J., & Jegen, M. (2010). Evaluation of gas hydrate deposits in an active seep area using marine controlled source electromagnetics: Results from Opouawe Bank, Hikurangi Margin, New Zealand. *Marine Geology*, *272*(1-4), 79–88. https://doi.org/10.1016/j.margeo.2009.07.006

Sen, P. N., Scala, C., & Cohen, M. H. (1981). A self-similar model for sedimentary rocks with application to the dielectric constant of fused glass. *Geophysics*, *36*(5), 781–795.

Spangenberg, E. (2001). Modeling of the influence of gas hydrate content on the electrical properties of porous sediments. *Journal of Geophysical Research*, *106*(B4), 6535–6548. https://doi.org/10.1029/2000JB900434

Spangenberg, E., & Kulenkampff, J. (2005). Physical properties of gas hydrate-bearing sediment. In *Fifth International Conference on Gas Hydrates*. Trondheim, Norway. 12–16 June.

Spangenberg, E., & Kulenkampff, J. (2006). Influence of methane hydrate content on electrical sediment properties. *Geophysical Research Letters*, *33*, L24315. https://doi.org/10.1029/2006GL028188

Swanson, B. F. (1985). Microporosity in reservoir rocks—It's measurement and influence on electrical resistivity. In *SPWLA 26th Annu. Logging Symp*.

Sweeney, S., & Jennings, H. (1960). Effect of wettability on the electrical resistivity of carbonate rock from a petroleum reservoir. *The Journal of Physical Chemistry*, *64*(5), 551–553. https://doi.org/10.1021/j100834a009

Takahashi, H., Fercho, E., & Dallimore, S. R. (2005). Drilling and operations overview of the Mallik 2002 production research well program. In S. R. Dallimore & T. S. Collett (Eds.) *Scientific results from the Mallik 2002 Gas Hydrate Production Research Well Program, Mackenzie Delta*, *Bulletin No. 585* (p. 16). Northwest Territories, Canada: Geological Survey of Canada.

Tohidi, B., Anderson, R., Clennell, M. B., Burgass, R. W., & Biderkab, A. B. (2001). Visual observation of gas-hydrate formation and dissociation in synthetic porous media by means of glass micromodels. *Geology*, *29*(9), 867–870. https://doi.org/10.1130/0091-7613(2001)029%3C0867:VOOGHF%3E2.0.CO;2

Uchida, E., Tsuji, T., Takahashi, T., Okui, T., & Minagawa, H. (2005). Petrophysical properties and sedimentology of gas-hydrate-bearing sediments in the JAPEX/JNOC/GSC et al. Mallik 5L-38 gas hydrate production research well. In S. R. Dallimore & T. S. Collett (Eds.), *Scientific results from the Mallik 2002 Gas Hydrate Production Research Well Program, Mackenzie Delta*, *Bulletin No. 585* (p. 16). Northwest Territories, Canada: Geological Survey of Canada.

Ussler, W. III, & Paull, C. K. (2001). Ion exclusion associated with marine gas hydrate deposits. In C. K. Paull & W. P. Dillon (Eds.), *Natural gas hydrates: Occurrence, distribution, and detection*, *Geophysical Monograph Series* (Vol. 124, pp. 41–51). Washington, DC: AGU.

Van Rensbergen, P., De Batist, M., Klerkx, J., Hus, R., Poort, J., Vanneste, M., et al. (2002). Sublacustrine mud volcanoes and methane seeps caused by dissociation of gas hydrates in Lake Baikal. *Geology*, *30*(7), 631. https://doi.org/10.1130/0091-7613(2002)030%3C0631:SMVAMS%3E2.0.CO;2

Waite, W. F., Santamarina, J. C., Cortes, D. D., Dugan, B., Espinoza, D. N., Germaine, J., et al. (2009). Physical properties of hydrate-bearing sediments. *Reviews of Geophysics*, *47*, RG4003. https://doi.org/10.1029/2008RG000279

Waite, W. F., Winters, W. J., & Mason, D. (2004). Methane hydrate formation in partially water-saturated Ottawa sand. *American Mineralogist*, *89*(8-9), 1202–1207. https://doi.org/10.2138/am-2004-8-906

Wallmann, K., Pinero, E., Burwicz, E., Haeckel, M., Hensen, C., Dale, A., & Ruepke, L. (2012). The global inventory of methane hydrate in marine sediments: A theoretical approach. *Energies*, *5*(12), 2449–2498. https://doi.org/10.3390/en5072449

Waxman, M. H., & Smits, L. J. M. (1968). Electrical conductivities in oil-bearing shaly sands. *Society of Petroleum Engineers Journal*, *8*(02), 107–122. https://doi.org/10.2118/1863-A

Weitemeyer, K., Constable, S., & Tréhu, A. (2011). A marine electromagnetic survey to detect gas hydrate at Hydrate Ridge, Oregon. *Geophysical Journal International*, *187*(1), 45–62. https://doi.org/10.1111/j.1365-246X.2011.05105.x

Wildenschild, D., Roberts, J. J., & Carlberg, E. D. (2000). On the relationship between microstructure and electrical and hydraulic properties of sand-clay mixtures. *Geophysical Research Letters*, *27*(19), 3085–3088. https://doi.org/10.1029/2000GL011553

Winsauer, W. O., & McCardell, W. M. (1953). Ionic double-layer conductivity in reservoir rock. *Journal of Petroleum Technology*, *5*(05), 129–134. https://doi.org/10.2118/953129-G

Winsauer, W. O., Shearin, H. M., Masson, P. H., & Williams, M. (1952). Resistivity of brine-saturated sands in relation to pore geometry. *AAPG Bulletin*, *36*(2), 253–277.

Winters, W. J., Dallimore, S. R., Collett, T. S., Medioli, B. E., Matsumoto, R., Katsube, T. J., & Brennan-Alpert, P. (2005). Relationships of sediment physical properties from the JAPEX/JNOC/GSC et al. Mallik 5L-38 Gas Hydrate Production Research Well. In S. R. Dallimore & T. S. Collett (Eds.), *Scientific results from the Mallik 2002 Gas Hydrate Production Research Well Program, MacKenzie Delta*, *Bulletin No. 585* (p. 9). Northwest Territories, Canada: Geological Survey of Canada.

Worthington, P. F. (1985). The evolution of shaley-sand concepts in reservoir evaluation. *The Log Analyst*, *26*(1), 23–40.

Wu, P., Lovell, J., Clark, B., Bonner, S., & Tabanou, J. (1999). *Dielectric-independent 2-MHz propagation resistivities*. Paper presented at the 1999 SPE Annual Technical Conference and Exhibition (Vol. 56448).

Yamamoto, K., Terao, Y., Fujii, T., Ikawa, T., Seki, M., Matsuzawa, M., & Kanno, T. (2014). Operational overview of the first offshore production test of methane hydrates in the Eastern Nankai Trough. *Offshore Technology Conference*, (OTC-25243-MS). https://doi.org/10.4043/25243-MS

Yoneda, J., Masui, A., Konno, Y., Jin, Y., Kida, M., Katagiri, J., et al. (2017). Pressure-core-based reservoir characterization for geomechanics: Insights from gas hydrate drilling during 2012–2013 at the eastern Nankai Trough. *Marine and Petroleum Geology*, *86*, 1–16. https://doi.org/10.1016/j.marpetgeo.2017.05.024

Yun, T. S., Francisca, F. M., Santamarina, J. C., & Ruppel, C. (2005). Compressional and shear wave velocities in uncemented sediment containing gas hydrate. *Geophysical Research Letters*, *32*, L10609. https://doi.org/10.1029/2005GL022607

Yun, T. S., Santamarina, J. C., & Ruppel, C. (2007). Mechanical properties of sand, silt, and clay containing tetrahydrofuran hydrate. *Journal of Geophysical Research*, *112*, B04106. https://doi.org/10.1029/2006JB004484